

Dynamical features and shadows of quantum Schwarzschild black hole in effective field theories of gravity

Zi-Liang Wang  ^{1*} and Emmanuele Battista  ^{2,3,4†}

¹ *Department of Physics, School of Science,
Jiangsu University of Science and Technology, Zhenjiang, 212003, China*

² *Quantum Theory Center (\hbar QTC) & D-IAS,
Southern Denmark University, Campusvej 55, 5230 Odense M, Denmark*

³ *Department of Physics “Ettore Pancini”, University of Naples “Federico II”,
Via Cintia Edificio 6, 80126 Naples, Italy*

⁴ *Istituto Nazionale di Fisica Nucleare,
Sezione di Napoli, University of Naples “Federico II”,
Via Cintia Edificio 6, 80126 Naples, Italy*

(Dated: January 27, 2025)

Abstract

We investigate the properties of the Schwarzschild black hole geometry involving leading one-loop long-distance quantum effects, which arise within the framework of effective field theories of gravity. Our analysis reveals that geodesic trajectories of both massive and massless particles can assume completely different behaviours depending on the sign assumed by the quantum contributions, in spite of their smallness. Moreover, we find that the positions of stable and unstable circular orbits are determined by an algebraic quartic equation, which we solve by developing a straightforward and analytic method. Additionally, we examine black hole shadows and rings by means of two different emission profile models, which account for quantum corrections to the innermost stable circular orbit and photon sphere radii. The Hawking temperature and the entropy of the black hole are also derived. Finally, we draw our conclusions.

* ziliang.wang@just.edu.cn

† ebattista@na.infn.it; emmanuelebattista@gmail.com

I. INTRODUCTION

Among the four fundamental forces of nature, gravity is the most intriguing. Indeed, despite having been the first to be studied, it remains the only interaction for which we have yet to provide a definitive quantum description. The main troubles in this regard can be traced back to the fact that general relativity is not (perturbatively) renormalizable in the traditional sense. This aspect can be accounted for in different ways. First of all, on dimensional grounds, a simple power counting argument shows that the Newton constant G carries the dimension of the inverse Planck mass squared (similarly to the Fermi model of weak interactions), while it is known that a renormalizable theory possesses a coupling constant with positive mass dimension [1]. Moreover, one-loop infinities of vacuum gravity involve quadratic combinations of the Ricci tensor, which are thus not proportional to the original Einstein-Hilbert Lagrangian [2]. The situation gets worse at two-loop level, where ultraviolet divergencies comprise cubic invariants of the Riemann tensor, and hence cannot be canceled even if Einstein field equations are employed [3]. This state of affairs can be readily explained thanks to the theorem illustrated in Ref. [4], which delineates the general form assumed by the leading L -loop divergencies of the quantum S matrix for pure gravity in d dimensions. The immediate consequence of this result is that the cancellation of ultraviolet infinities would require the introduction in the counter-Lagrangian of an infinite number of contributions, which are proportional to arbitrarily high powers of the Riemann curvature tensor and its covariant derivatives, and hence not present in the Einstein-Hilbert Lagrangian.

To address this unsatisfactory scenario, some competing quantum formulations of gravity have been put forward thus far. The most promising frameworks are loop quantum gravity, which represents a background-independent and nonperturbative approach [5, 6], and string theory, which relies on both perturbative and nonperturbative techniques and has the ambitious scope of unifying all known fundamental physics into one single paradigm [7–9]. Other research programs worth mentioning are: twistor theory [10], noncommutative geometry [11, 12], Euclidean quantum gravity [13, 14], causal dynamical triangulation [15], and casual set theory [16]. However, despite these efforts, a comprehensive and viable quantum gravity model is still missing. One way to overcome this issue consists in resorting to the tools of effective field theories (EFTs), which permit treating general relativity as a well-behaved

quantum theory at energies far below the Planck mass [17–25]. Gravity naturally adheres to the EFT pattern. The main concept is that, after having integrated heavy particles out of the theory, the remaining massless (or, in general, very light) fields will be described by the most general effective Lagrangian which is invariant under the action of the diffeomorphism group. This Lagrangian function can then be ordered in an energy expansion, where the leading low-energy interactions stem from the Einstein-Hilbert piece and can be used in a full field-theoretic manner to make physical predictions. Indeed, the Ricci scalar occurring in the Einstein-Hilbert action contains second-order derivatives of the metric, which become quadratic in the four-momentum $p_\mu \sim i\partial_\mu$ when translated in momentum space. On the other hand, higher-order terms are at least quartic in p_μ and hence are suppressed at low energy. The key strength of the EFT scheme thus lies in the fact that it can be employed even if the high-energy completion of quantum gravity remains unknown. Indeed, the only residual effects of high-energy contributions appear, at low-energy scales, in the form of a shift of a few parameters in the Lagrangian whose (renormalized) values can be determined experimentally.

By means of the EFT formalism, it has been possible to derive the leading one-loop long-distance quantum corrections to the Newtonian gravitational potential [17, 26–30], as well as the principal known solutions of Einstein field equations [31, 32], and subsequently many applications, both at classical and quantum level, of these results have been considered in the literature [33–57]. Motivated by the enormous complexity of the calculations involved (see e.g. Refs. [58, 59]), EFT techniques have been recently combined with on-shell unitarity methods [60], unveiling interesting outcomes in the field of scattering amplitudes and their relation to classical gravity [61–65].

Another topic which has garnered attention concerns the study of the deformations and quantum aspects of black holes, drawing from either fundamental or extended gravity patterns, EFT approaches, and different quantum gravity models (see e.g. Refs. [66–90]). Indeed, such investigations can give insights into the interplay between general relativity and quantum mechanics, providing a unique quantum gravity testing ground; moreover, the examination of these geometries offers the possibility of sorting out the issue of classical spacetime singularities, furnish crucial clues to understanding the behavior of the early universe [91], and give hints for resolving the black hole information paradox [92].

Recently, we have delved into the quantum Schwarzschild solution within the EFT pattern

[93]. Our study has been carried out upon constructing a coordinate transformation relating the harmonic coordinates originally employed in Ref. [32] and the Schwarzschild ones. To take into account the discordant results existing in the literature (see e.g. Table 1 in Ref. [72]), the one-loop quantum corrections have been written in their most general form in terms of a factor k_1 , and we have found that the metric components are such that $-g_{tt} \neq g^{rr}$. This relation has led to several interesting implications not present at classical level, such as the possible occurrence of a Penrose-like energy-extraction mechanism violating the null energy condition (NEC). In this paper, we further explore the features of the quantum Schwarzschild geometry. Specifically, we analyze the behaviour of both timelike and null geodesics, as well as the black hole appearance and its emission properties. The plan of the paper is as follows. We begin with an outline of the main properties and the thermodynamic aspects of the quantum Schwarzschild solution in Sec. II. After that, the influence of the quantum effects on the dynamics of freely falling particles is examined in Sec. III, where we also show that the positions of stable and unstable circular orbits are ruled by a quartic equation, for which we devise a simple and analytic resolution method. The findings of this section are then exploited to deal with shadows and rings of the quantum black hole in Sec. IV. We finally draw our conclusions in Sec. V.

II. THE QUANTUM SCHWARZSCHILD GEOMETRY

Within the EFT paradigm, it is possible to work out the leading low-energy one-loop quantum corrections to the Schwarzschild metric [32]. The underlying calculations, which can be performed either by means of the traditional Feynman diagrammatic rules or the modern on-shell unitarity methods [60], involve harmonic coordinates. By constructing a coordinate transformation to the standard Schwarzschild coordinates $\{ct, r, \theta, \phi\}$, the quantum Schwarzschild metric can be written as follows [93]

$$ds^2 = g_{\mu\nu} dx^\mu dx^\nu = -B(r) (c^2 dt^2) + A(r) dr^2 + r^2 d\Omega^2, \quad (1a)$$

with $d\Omega^2 = d\theta^2 + \sin^2\theta d\phi^2$ and

$$B(r) = 1 - \frac{R_S}{r} + \frac{k_1}{2} \frac{R_S \ell_P^2}{r^3} + \mathcal{O}(r^{-4}), \quad (1b)$$

$$A(r) = \left(1 - \frac{R_S}{r}\right)^{-1} - \frac{3k_1}{2} \frac{R_S \ell_P^2}{r^3} + \mathcal{O}(r^{-4}), \quad (1c)$$

$R_S = 2GM/c^2$ and $\ell_P = (G\hbar/c^3)^{1/2}$ being the Schwarzschild radius and Planck length, respectively. In the above equations, the remainder $\mathcal{O}(r^{-4})$ indicates two-loop quantum terms and will be hereafter omitted. Moreover, k_1 is the dimensionless real-valued parameter embodying the quantum contributions; since the literature provides different and sometimes discordant assessments, we will leave k_1 general; however, we note that its typical values are such that (see e.g. Table 1 in Ref. [72])

$$|k_1| \sim \mathcal{O}(1). \quad (2)$$

It has been demonstrated in Ref. [60] that the quantum contributions appearing in Eq. (1) have a universal character, in the sense that they are to be expected in any quantum gravity theory with the same low-energy degrees of freedom as those considered in this paper.

As explained in Ref. [93], the validity of the EFT scheme requires that

$$R_S \gg \ell_P, \quad (3)$$

or, equivalently,

$$M \gg \frac{1}{2} M_P, \quad (4)$$

where $M_P = (\hbar c/G)^{1/2}$ denotes Planck mass. In fact, these relations guarantee that in our model the one-loop modifications to the standard classical outcomes do not become arbitrarily large. In this way, our results can always be written as a classical piece amended by a small quantum factor.

One of the peculiarities of the metric (1) is that $-g_{tt} \neq g^{rr}$. This condition gives rise to some interesting features which will be discussed in Secs. IIA and IIB (for further details, including the description of a possible energy-extraction mechanism, we refer the reader to Ref. [93]). We conclude this section with an analysis of the effective energy-

momentum tensor underlying the quantum Schwarzschild black hole and a first account of its thermodynamic properties in Secs. [II C](#) and [II D](#), respectively.

A. Metric horizons and null hypersurfaces

The horizons of the quantum spacetime [\(1\)](#) can be obtained from the condition $g_{tt} = 0$. By solving the ensuing algebraic cubic equation $r^3 - R_S r^2 + \frac{1}{2} k_1 R_S \ell_P^2 = 0$, we find that when k_1 is positive and $M > M^*$ (with $M^* := M_P \sqrt{\frac{27}{32} k_1}$), the Schwarzschild metric admits two horizons whose radii are

$$\begin{aligned} r_1 &= \frac{2}{3} R_S \cos \left\{ \frac{1}{3} \arccos \left[1 - \frac{27}{4} k_1 \left(\frac{\ell_P}{R_S} \right)^2 \right] \right\} + \frac{1}{3} R_S \\ &= R_S \left[1 - \frac{k_1 \ell_P^2}{2 R_S^2} + \mathcal{O}(\ell_P^4/R_S^4) \right], \end{aligned} \quad (5)$$

$$\begin{aligned} r_2 &= -\frac{2}{3} R_S \sin \left\{ \frac{\pi}{6} - \frac{1}{3} \arccos \left[1 - \frac{27}{4} k_1 \left(\frac{\ell_P}{R_S} \right)^2 \right] \right\} + \frac{1}{3} R_S \\ &= \ell_P \sqrt{\frac{k_1}{2}} + \mathcal{O}(\ell_P^2/R_S). \end{aligned} \quad (6)$$

On the other hand, when $k_1 < 0$, then for any real-valued M there exists one metric horizon only with radius

$$\begin{aligned} r_3 &= \frac{1}{3} R_S + \frac{1}{3} R_S \left[1 - \frac{27}{4} k_1 \left(\frac{\ell_P}{R_S} \right)^2 + 3\sqrt{3} \sqrt{\frac{k_1}{2} \left(\frac{\ell_P}{R_S} \right)^2 \left(k_1 \frac{27}{8} \frac{\ell_P^2}{R_S^2} - 1 \right)} \right]^{-1/3} \\ &+ \frac{1}{3} R_S \left[1 - \frac{27}{4} k_1 \left(\frac{\ell_P}{R_S} \right)^2 + 3\sqrt{3} \sqrt{\frac{k_1}{2} \left(\frac{\ell_P}{R_S} \right)^2 \left(k_1 \frac{27}{8} \frac{\ell_P^2}{R_S^2} - 1 \right)} \right]^{1/3} \\ &= R_S \left[1 - \frac{k_1 \ell_P^2}{2 R_S^2} + \mathcal{O}(\ell_P^4/R_S^4) \right]. \end{aligned} \quad (7)$$

It is worth noting that Eqs. [\(5\)](#)–[\(7\)](#) have been obtained by exploiting the constraint [\(3\)](#); moreover, as a consequence of Eqs. [\(2\)](#) and [\(3\)](#), the horizons [\(5\)](#) and [\(6\)](#) meet the inequality

$$r_2 \ll r_1. \quad (8)$$

Let there be given in the spacetime geometry (1) an hypersurface, say Σ , having constant radius and normal vector n^μ . Σ becomes null when

$$g_{\mu\nu}n^\mu n^\nu = g^{rr} = 0, \quad (9)$$

where, owing to Eq. (1c) and up to $O(r^{-4})$ terms,

$$g^{rr} = 1 - \frac{R_S}{r} + \frac{3}{2}k_1 \frac{R_S \ell_P^2}{r^3}. \quad (10)$$

In the standard Schwarzschild geometry, where $k_1 = 0$, the condition $g^{rr} = 0$ is equivalent to $g_{tt} = 0$. Therefore, the (event) horizon located at $r = R_S$ is automatically a null hypersurface, i.e., the place where nothing, not even light, can escape from. This circumstance is no longer true in the Schwarzschild geometry (1), since, as pointed out before, g^{rr} is different from $-g_{tt}$. Therefore, a null hypersurface Σ does not coincide with any of the metric horizons analyzed before. In fact, the relation (9) leads to the new algebraic third-order equation $r^3 - r^2 R_S + \frac{3}{2}k_1 R_S \ell_P^2 = 0$, which admits two real positive roots when $k_1 > 0$ and $M > \sqrt{3}M^*$, and one real positive solution whenever k_1 is negative. In the first scenario, upon employing Eq. (3), the radii of the null hypersurfaces Σ_1 and Σ_2 are found to be

$$\tilde{r}_1 = R_S \left[1 - \frac{3k_1}{2} \frac{\ell_P^2}{R_S^2} + O(\ell_P^4/R_S^4) \right], \quad (11)$$

$$\tilde{r}_2 = \ell_P \sqrt{\frac{3k_1}{2}} + O(\ell_P^2/R_S), \quad (12)$$

respectively. In our hypotheses, we have

$$\tilde{r}_2 \ll \tilde{r}_1, \quad (13)$$

along with

$$\tilde{r}_1 < r_1 < R_S, \quad (14)$$

$$\tilde{r}_2 > r_2. \quad (15)$$

The positions of the metric horizons (5) and (6) and the null hypersurfaces Σ_1 and Σ_2 are drawn in Fig. 1.

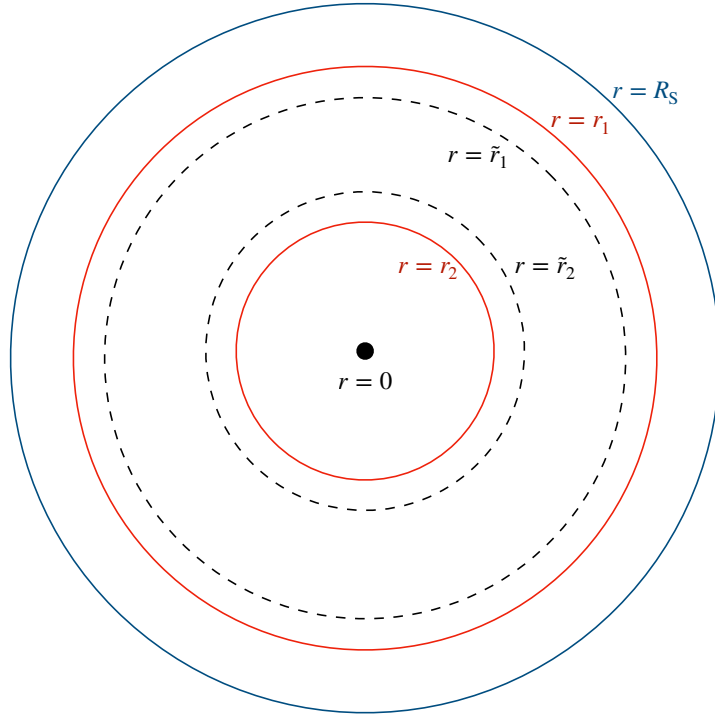


FIG. 1: Pictorial representation of the Schwarzschild radius, horizons located at $r = r_1$ and $r = r_2$, and null hypersurfaces Σ_1 and Σ_2 in the case $k_1 > 0$.

When $k_1 < 0$, the null hypersurface Σ_3 is characterized by the radius

$$\tilde{r}_3 = R_S \left[1 - \frac{3k_1}{2} \frac{\ell_P^2}{R_S^2} + \mathcal{O}(\ell_P^4/R_S^4) \right], \quad (16)$$

and satisfies (cf. Eq. (7))

$$\tilde{r}_3 > r_3 > R_S. \quad (17)$$

The main features of the framework having negative k_1 are shown in Fig. 2.

The study of the sign of g^{rr} reveals that [93]

$$r < \tilde{r}_2 : \quad g^{rr} > 0, \quad (18a)$$

$$\tilde{r}_2 < r < \tilde{r}_1 : \quad g^{rr} < 0, \quad (18b)$$

$$r > \tilde{r}_1 : \quad g^{rr} > 0, \quad (18c)$$

which entails that all hypersurfaces Σ whose radius is smaller than \tilde{r}_2 or larger than \tilde{r}_1 are timelike and hence can be crossed by a particle either inwards or outwards [94]; moreover,

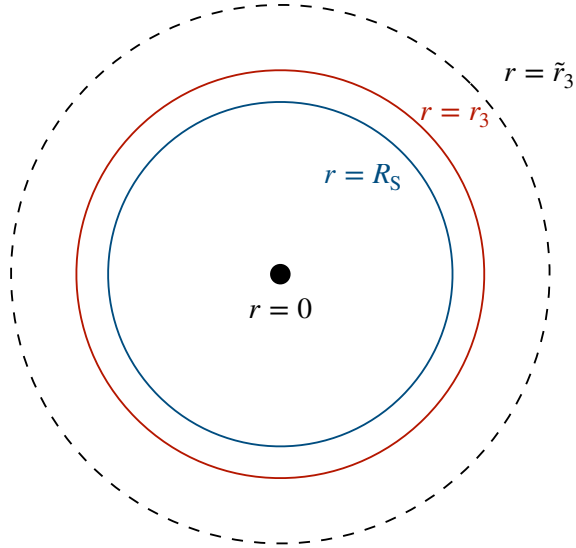


FIG. 2: Pictorial representation of the null hypersurface Σ_3 , horizon located at $r = r_3$, and Schwarzschild radius in the case $k_1 < 0$.

the hypersurfaces Σ having a radius lying in the interval $\tilde{r}_2 < r < \tilde{r}_1$ are spacelike, i.e., they can be crossed by a particle in one direction only [94]. On the other hand, in the case $k_1 < 0$, we have the following situation:

$$r < \tilde{r}_3 : \quad g^{rr} < 0, \quad (19a)$$

$$r > \tilde{r}_3 : \quad g^{rr} > 0, \quad (19b)$$

which means that the hypersurfaces Σ are spacelike if $r < \tilde{r}_3$, while they are timelike otherwise.

B. Change of signature

Among the peculiarities of the quantum Schwarzschild metric (1), we also remark the fact that its signature is allowed to change within some Planck-scale domains.

In the scenario having positive k_1 , g_{tt} is negative if $r < r_2$ or $r > r_1$, while it attains positive values otherwise [93]; thus, bearing in mind Eq. (18), we see that $g_{\mu\nu}$ assumes the Euclidean (i.e., Riemannian) signature (++++) when $r_2 < r < \tilde{r}_2$ and $\tilde{r}_1 < r < r_1$ (see Fig. 1). On the other hand, if k_1 is negative, the temporal component g_{tt} is positive (resp. negative) if $r < r_3$ (resp. $r > r_3$) [93], which, owing to Eq. (19), implies that the metric

admits the ultrahyperbolic signature $(- - ++)$ for $r_3 < r < \tilde{r}_3$ (see Fig. 2).

This behaviour of the metric can be ascribed to its quantum nature, which becomes more significant in the aforementioned Planck-extent regions. This point is also suggested by a comparison with some existing and well-studied quantum models. In fact, the regime with $k_1 > 0$ is reminiscent of the change-of-signature idea featured in quantum cosmology, where the spacetime metric experiences a signature transition from Euclidean to Lorentzian at the beginning of the cosmological evolution (see e.g. Refs. [95, 96]); a similar pattern is also exploited in other fields, such as loop quantum gravity [97], supergravity and string theory [98–100]. The framework with negative k_1 shares some similarities with a class of theories having two time dimensions, known as two-time or 2T physics, which finds application in classical and quantum physics including field theories, gravity, and cosmology (see e.g. Refs. [101–104] and references therein).

C. Effective energy-momentum tensor

The quantum Schwarzschild metric (1) can be interpreted as a non-vacuum solution of the Einstein field equations. In this context, quantum contributions can be associated with the presence of an effective stress-energy tensor that permits gaining insights into the physical aspects of the underlying matter fields. This approach enables in general a deeper understanding of the interplay between quantum effects and classical geometry, shedding light on the properties of spacetimes involving one-loop quantum modifications.

In order to perform our investigation, we extend the metric given in Eq. (1) as follows:

$$ds^2 = \tilde{g}_{\mu\nu} dx^\mu dx^\nu = -\tilde{B}(r) (c^2 dt^2) + \tilde{A}(r) dr^2 + r^2 d\Omega^2, \quad (20a)$$

with

$$\tilde{B}(r) = 1 - \frac{R_S}{r} + \frac{k_1 R_S \ell_P^2}{2 r^3} + \frac{f_b k_1 R_S^2 \ell_P^2}{r^4} + \mathcal{O}(r^{-5}), \quad (20b)$$

$$\tilde{A}(r) = \left(1 - \frac{R_S}{r}\right)^{-1} - \frac{3k_1 R_S \ell_P^2}{2 r^3} + \frac{f_a k_1 R_S^2 \ell_P^2}{r^4} + \mathcal{O}(r^{-5}), \quad (20c)$$

where the explicit value of the constants f_a and f_b entering the (leading) two-loop quantum corrections will not impact our examination. Starting from Eq. (20), one could derive the

corresponding Einstein tensor $E_{\mu\nu}$, defined as usual as

$$E_{\mu\nu} = R_{\mu\nu} - \frac{1}{2}g_{\mu\nu}R. \quad (21)$$

Considering the leading-order factors in ℓ_{P}^2 , the $t-t$ and $r-r$ components of $E_{\mu\nu}$ read as, respectively,

$$E_{tt} = \frac{3k_1 R_S \ell_{\text{P}}^2}{r^5} - \frac{3k_1 R_S^2 \ell_{\text{P}}^2 (f_a + 4)}{r^6} + \frac{k_1 R_S^3 \ell_{\text{P}}^2 (11f_a + 15)}{r^7} - \frac{k_1 R_S^4 \ell_{\text{P}}^2 (13f_a + 6)}{r^8} + \frac{5f_a k_1 R_S^5 \ell_{\text{P}}^2}{r^9}, \quad (22a)$$

$$E_{rr} = -\frac{2k_1 R_S^2 \ell_{\text{P}}^2 (2f_b + 1)}{r^4 (r - R_S)^2} + \frac{3k_1 R_S^3 \ell_{\text{P}}^2 (2f_b + 1)}{2r^5 (r - R_S)^2} - \frac{f_a k_1 R_S^2 \ell_{\text{P}}^2}{r^6}. \quad (22b)$$

From the above formulas, it is evident that if we neglect two-loop $O(r^{-4})$ contributions in Eq. (20) (as we did in Eq. (1)), only the first factor on the right-hand side of Eq. (22a) should be retained, while all terms occurring in the expression (22b) of E_{rr} should be discarded. By applying the same procedure also to $E_{\theta\theta}$ and $E_{\phi\phi}$ while keeping again the one-loop accuracy in the metric (20), we find that these vanish. Therefore, the final form of $E_{\mu\nu}$ turns out to be

$$E_{tt} = \frac{3k_1 R_S \ell_{\text{P}}^2}{r^5}, \quad (23a)$$

$$E_{rr} = E_{\theta\theta} = E_{\phi\phi} = 0, \quad (23b)$$

which represents the correct Einstein tensor if one starts from the one-loop corrected geometry (1). Assuming that the Einstein gravitational field equations still hold in this situation, namely

$$E_{\mu\nu} = \frac{8\pi G}{c^4} T_{\mu\nu}, \quad (24)$$

then from Eq. (23) we arrive at the corresponding effective energy-momentum tensor:

$$T_{\mu\nu} = \frac{3k_1 c^4 R_S \ell_{\text{P}}^2}{8\pi G r^5} \text{diag}(1, 0, 0, 0). \quad (25)$$

As a self-consistency check, one can verify that $T_{\mu\nu}$ is conserved up to higher-order contributions.

The knowledge of the effective energy-momentum tensor allows us to evaluate an impor-

tant physical quantity like the effective energy density

$$\rho = -T_t{}^t = \frac{3k_1\ell_{\text{P}}^2c^4R_{\text{S}}}{8\pi Gr^5}, \quad (26)$$

which we have written in such a way as to be identical to the energy density measured by a static observer in her/his local “proper reference frame” [105]. It is thus clear that ρ is always negative if $k_1 < 0$, a condition which points out that the weak energy condition fails to hold [106]. Moreover, we can also determine if the NEC is respected. For this reason, let us introduce the null vector

$$k^\mu = \left(1/\tilde{B}, \pm 1/\sqrt{\tilde{A}\tilde{B}}, 0, 0\right), \quad (27)$$

which points in the outgoing or ingoing radial direction, depending on whether the plus or minus sign is chosen, respectively. Owing to Eqs. (25) and (27), we obtain

$$T_{\mu\nu}k^\nu k^\nu = \frac{3k_1\ell_{\text{P}}^2c^4R_{\text{S}}}{8\pi Gr^5(1 - R_{\text{S}}/r)^2} + \mathcal{O}(r^{-6}), \quad (28)$$

and hence we can conclude, modulo higher-order factors, that the NEC is contravened for negative k_1 .

The NEC violation is a phenomenon that typically characterizes physical systems involving quantum processes, and as such, it is expected to occur also in the quantum Schwarzschild geometry we are studying. Our investigation shows that, at this order, the NEC is satisfied for positive k_1 , but the situation may change when next-to-leading-order terms are taken into account. For instance, if we just write $f_{\text{b}} = \lambda f_{\text{a}}$ (with $\lambda \in \mathbb{R}$) in Eq. (20), then the NEC could be breached also when k_1 is positive for $r < [14 + 4(1 + \lambda)f_{\text{a}}]R_{\text{S}}/3$. Therefore, we can say that the calculations carried out in this section represent a direct proof of the NEC infringement in the scenario having negative k_1 , while an indirect evidence that NEC is broken when $k_1 > 0$ is provided by the existence of the Penrose-like energy-extraction mechanism discussed in Ref. [93]. We will return to this point in Sec. III B 1.

A final remark is now in order. The analysis of Ref. [32] has demonstrated how the Schwarzschild metric can be derived at one-loop level, starting from the energy-momentum tensor of a source that contains the contributions of both the classical gravitational field

and its quantum fluctuations. Alternatively, in our approach, the metric (20) consists of the exact ordinary classical piece plus small quantum corrections. As a result, the effective energy-momentum tensor (25) (or equivalently the Einstein tensor (23)) is a fully quantum object, where, differently from Ref. [32], no classical factors are present.

D. Thermodynamic aspects

Having outlined the general features of the quantum geometry (1), we now provide a first examination of its thermodynamic aspects. Specifically, we compute the black hole entropy using two approaches: one relying on the Hawking temperature (see Sec. IID 1) and the other on the Wald formula (see Sec. IID 2).

1. Hawking temperature

The Hawking temperature T_H is a fundamental concept in black hole thermodynamics that reflects the interaction between gravity and quantum field theory in curved spacetimes [107]. It can be formally expressed as [106]

$$T_H = \frac{\hbar}{ck_B} \frac{\kappa}{2\pi}, \quad (29)$$

κ being the surface gravity. In a spherically symmetric spacetime, we can write

$$\kappa^2 = c^4 \left[-\frac{1}{2} (\nabla_\mu \xi_\nu) (\nabla^\mu \xi^\nu) \right]_{r=r_H} = c^4 \left[-\frac{1}{4} \frac{1}{g_{rr}g_{tt}} (g'_{tt})^2 \right]_{r=r_H}, \quad (30)$$

where $\xi^\mu = \delta^{\mu 0}$ denotes the static Killing vector field, the prime the derivative with respect to r , and r_H the horizon radius, which in our setup is located at r_1 when $k_1 > 0$ and at r_3 if $k_1 < 0$. It follows from Eqs. (1b) and (1c), that

$$-\frac{1}{4} \frac{1}{g_{rr}g_{tt}} (g'_{tt})^2 = \frac{R_S^4}{4} \left[\frac{1}{R_S^2} \frac{1}{r^4} - 3k_1 \frac{\ell_P^2}{R_S^2} \frac{1}{r^6} + \mathcal{O}(r^{-7}) \right], \quad (31)$$

which, in view of Eqs. (5) and (7), yields

$$T_{\text{H}} = \frac{\hbar c}{k_{\text{B}}} \frac{1}{4\pi R_{\text{S}}} \left[1 - \frac{k_1}{2} \frac{\ell_{\text{P}}^2}{R_{\text{S}}^2} + \text{O}(\ell_{\text{P}}^4/R_{\text{S}}^4) \right], \quad (32)$$

where we have taken into account the condition (3). If we now use the first law of thermodynamics $c^2 dM = T_{\text{H}} d\mathcal{S}$, we then obtain that the entropy is given by, modulo higher-order corrections,

$$\mathcal{S} = c^2 \int \frac{dM}{T_{\text{H}}(M)} = \frac{\pi k_{\text{B}} c^3}{\hbar G} R_{\text{S}}^2 \left[1 + k_1 \frac{\ell_{\text{P}}^2}{R_{\text{S}}^2} \log\left(\frac{R_{\text{S}}}{\ell_{\text{P}}}\right) \right]. \quad (33)$$

This equation suggests that ℓ_{P} , or equivalently M_{P} , can be seen as a natural cutoff for the model, consistently with the EFT paradigm (a similar consideration will be taken into account in Sec. III A 2).

Let us notice that, remarkably, a correction to the entropy involving a logarithmic term is present also in the general formulas worked out in Ref. [82], and it is expected to be a general feature of EFT black hole models (see e.g. Refs. [79, 108–111]).

2. Wald entropy formula

We can now calculate the black hole entropy \mathcal{S} using the renowned Wald formula [107, 112, 113]. In this framework, \mathcal{S} is elegantly determined through an integral expression involving the Noether charge associated with the diffeomorphism invariance of a general gravity model. Specifically, for a diffeomorphism-invariant action

$$\mathcal{I} = \int d^4x \sqrt{-g} \mathcal{L}(g_{\alpha\beta}, R_{\mu\nu\rho\sigma}, \nabla_{\delta} R_{\mu\nu\rho\sigma}, \Psi, \nabla_{\delta} \Psi), \quad (34)$$

with Ψ the collection of matter fields in the theory and $R_{\mu\nu\rho\sigma}$ the Riemann tensor, the entropy is given by

$$\mathcal{S} = -2\pi \frac{k_{\text{B}}}{\hbar c} \int_{r=r_{\text{H}}} d\Sigma \epsilon_{\mu\nu} \epsilon_{\rho\sigma} \frac{\delta \mathcal{L}}{\delta R_{\mu\nu\rho\sigma}}, \quad (35)$$

where, for a spherically symmetric and static spacetime, $d\Sigma = r^2 \sin\theta d\theta d\phi$, and $\epsilon_{\mu\nu}$ is an antisymmetric tensor, normalized to $\epsilon_{\mu\nu} \epsilon^{\mu\nu} = -2$, whose nonvanishing component is

$\epsilon_{tr} = \sqrt{AB}$ (cf. Eq. (1))¹.

The action suitable for the EFT treatment of general relativity includes both local higher-order curvature corrections to the Einstein-Hilbert Lagrangian and nonlocal contributions, and thus reads as [17, 74]

$$\begin{aligned} \mathcal{I}_{\text{EFT}} = \int d^4x \sqrt{-g} & \left[\chi R + c_1 R^2 + c_2 R_{\alpha\beta} R^{\alpha\beta} + c_3 R_{\alpha\beta\epsilon\omega} R^{\alpha\beta\epsilon\omega} + \mathcal{L}_m \right. \\ & \left. - \vartheta R_{\alpha\beta\epsilon\omega} \log(\square/\varrho^2) R^{\alpha\beta\epsilon\omega} + \dots \right], \end{aligned} \quad (36)$$

where $\chi = c^4 (16\pi G)^{-1}$, $c_{1,2,3}$ and ϑ are constants, $\square := g^{\mu\nu} \nabla_\mu \nabla_\nu$ denotes the d'Alembertian operator, \mathcal{L}_m the matter Lagrangian, ϱ^{-1} a reference length scale, and the dots indicate higher-order modifications. The nonlocal factor involving $\log(\square/\varrho^2)$ is responsible for the logarithmic term occurring in Eq. (33). In fact, applying the Wald formula (35) to the EFT action (36) we find that the entropy of the quantum Schwarzschild black hole takes the form

$$\begin{aligned} \mathcal{S} = \frac{8\pi^2 k_B}{\hbar c} r_H^2 & \left\{ 2\chi + 4c_1 (R)_{r_H} - 2c_2 (R_\mu{}^\rho \epsilon^{\mu\sigma} \epsilon_{\rho\sigma})_{r_H} \right. \\ & \left. - 2(\epsilon_{\mu\nu} \epsilon_{\rho\sigma} R^{\mu\nu\rho\sigma})_{r_H} [c_3 + 2\vartheta(\gamma_E - 1) + \vartheta \log(r_H^2 \varrho^2)] \right\}, \end{aligned} \quad (37)$$

where the functional derivatives have been evaluated by resorting to the relation (see Appendix L in Ref. [114] for a glossary of functional differentiation formulas)

$$\frac{\delta R_{\alpha\beta\gamma\xi}}{\delta R_{\mu\nu\rho\sigma}} = \frac{1}{4} (\delta_\alpha^\mu \delta_\beta^\nu - \delta_\alpha^\nu \delta_\beta^\mu) (\delta_\gamma^\rho \delta_\xi^\sigma - \delta_\gamma^\sigma \delta_\xi^\rho), \quad (38)$$

and the last term follows from the identity

$$\log(\square/\varrho^2) R^{\alpha\beta\epsilon\omega} = -R^{\alpha\beta\epsilon\omega} [\log(r^2 \varrho^2) + 2(\gamma_E - 1)], \quad (39)$$

γ_E being the Euler-Mascheroni constant (see e.g. Refs. [71, 74, 79, 111] for further details

¹ Strictly speaking, Wald formula applies to bifurcate Killing horizons of stationary black holes and $\epsilon_{\mu\nu}$ is the binormal vector to the bifurcation surface.

on the derivation of Eq. (39)). Then, owing to the relations (cf. Eqs. (5) and (7))

$$(r^2 R)_{r_H} = \left[\frac{3k_1 \ell_P^2 R_S}{r^3} + O(r^{-4}) \right]_{r_H} = 3k_1 \frac{\ell_P^2}{R_S^2} + O(\ell_P^4/R_S^4), \quad (40a)$$

$$(r^2 R_\mu{}^\rho \epsilon^{\mu\sigma} \epsilon_{\rho\sigma})_{r_H} = \left[\frac{19k_1 \ell_P^2 R_S^2}{2r^4} + O(r^{-5}) \right]_{r_H} = \frac{19k_1 \ell_P^2}{2R_S^2} + O(\ell_P^4/R_S^4), \quad (40b)$$

$$(r^2 \epsilon_{\mu\nu} \epsilon_{\rho\sigma} R^{\mu\nu\rho\sigma})_{r_H} = \left[-\frac{4R_S}{r} + \frac{12k_1 R_S \ell_P^2}{r^3} + O(r^{-4}) \right]_{r_H} = -4 + \frac{10k_1 \ell_P^2}{R_S^2} + O(\ell_P^4/R_S^4), \quad (40c)$$

we obtain from Eq. (37)

$$\begin{aligned} \mathcal{S} = \frac{8\pi^2 k_B}{\hbar c} R_S^2 \left\{ 2\chi \left[1 - \frac{k_1 \ell_P^2}{R_S^2} + O(\ell_P^4/R_S^4) \right] + \frac{k_1 \ell_P^2}{R_S^4} (12c_1 - 19c_2) + \left[8/R_S^2 - 20k_1 \ell_P^2/R_S^4 \right. \right. \\ \left. \left. + O(\ell_P^4/R_S^6) \right] [c_3 + 2\vartheta(\gamma_E - 1) + \vartheta \log(r_H^2 \varrho^2)] + O(\ell_P^4/R_S^6) \right\}. \end{aligned} \quad (41)$$

Since the Planck length is expected to be the characteristic scale of the ultimate theory of quantum gravity, we can set $\varrho^2 \equiv \ell_P^{-2}$. Discarding higher-order corrections, we thus obtain

$$\mathcal{S} = \frac{\pi k_B c^3}{\hbar G} R_S^2 \left\{ 1 + \frac{4}{\chi R_S^2} [c_3 + 2\vartheta(\gamma_E - 1)] + \frac{8\vartheta}{\chi} \frac{1}{R_S^2} \log\left(\frac{R_S}{\ell_P}\right) \right\}, \quad (42)$$

which implies that the sought-after expression (33) for the entropy is recovered if

$$\begin{aligned} c_3 &= -2\vartheta(\gamma_E - 1), \\ \vartheta &= \frac{k_1 \ell_P^2}{8} \chi, \end{aligned} \quad (43)$$

while c_1 and c_2 can assume any value since they are related to terms yielding, at this level, negligible corrections. We notice that, remarkably, our final result aligns with the outcomes of e.g. Ref. [79].

A final remark deserves mention. The approach followed in this section does not represent the only way to derive the entropy formula (33). For instance, the class of local operators of the type $R_{\alpha\beta} \log(\square/\varrho^2) R^{\alpha\beta}$ or $R \log(\square/\varrho^2) R$ can also enter \mathcal{I}_{EFT} and lead to the logarithmic

factor in \mathcal{S} . Nonetheless, the calculations presented here serve as a valuable double-check of the effectiveness of this contribution.

III. GEODESIC DYNAMICS OF MASSIVE AND MASSLESS PARTICLES

The geodesic path of a freely falling particle moving in the equatorial plane of the quantum geometry (1) can be described starting from the equation (hereafter, we set $c = 1$) [93]

$$\frac{1}{2}\dot{r}^2 + \frac{1}{2} \frac{1}{A(r)} \left(\frac{L^2}{r^2} + \alpha \right) = \frac{1}{2} \frac{\mathcal{E}^2}{A(r)B(r)}, \quad (44)$$

where the dot stands for differentiation with respect to the affine parameter, and $\alpha = 0, 1$. The case $\alpha = 1$ refers to timelike geodesics, where the constants of motion \mathcal{E} and L represent the energy and angular momentum per unit rest mass of a massive particle, respectively; $\alpha = 0$ pertains to null geodesics, for which \mathcal{E} and L denote the total energy and angular momentum of a photon, respectively. Once the terms beyond one loop (i.e., those of the order $O(r^{-4})$) are neglected, Eq. (44) yields

$$\frac{1}{2}\dot{r}^2 + V_{\text{eff}}(r) = \frac{1}{2}\mathcal{E}^2, \quad (45)$$

where the quantum corrected effective potential is given by

$$V_{\text{eff}}(r) = \frac{1}{2} \left(1 - \frac{R_S}{r} \right) \left(\frac{L^2}{r^2} + \alpha \right) + \frac{1}{2} k_1 \left(\frac{3\alpha}{2} - \mathcal{E}^2 \right) \frac{R_S \ell_P^2}{r^3}. \quad (46)$$

The behavior of $V_{\text{eff}}(r)$ for both massive and massless particles is displayed in Figs. 3 and 4, respectively. Here, we have defined the impact parameter as $b := L/\mathcal{E}$, with its physical significance to be discussed in Sec. IV. For the chosen parameters, we see that the quantum effective potential exhibits differences compared to the classical Schwarzschild black hole case that become more pronounced as b decreases. This aligns with our expectations, since smaller values of b correspond to particles getting closer to the black hole and experiencing the strong-field regime, where quantum contributions gain importance.

At this point, some comments are in order. It is clear that Eq. (44) receives some divergent contributions which can be interpreted as an infinite-depth barrier as soon as

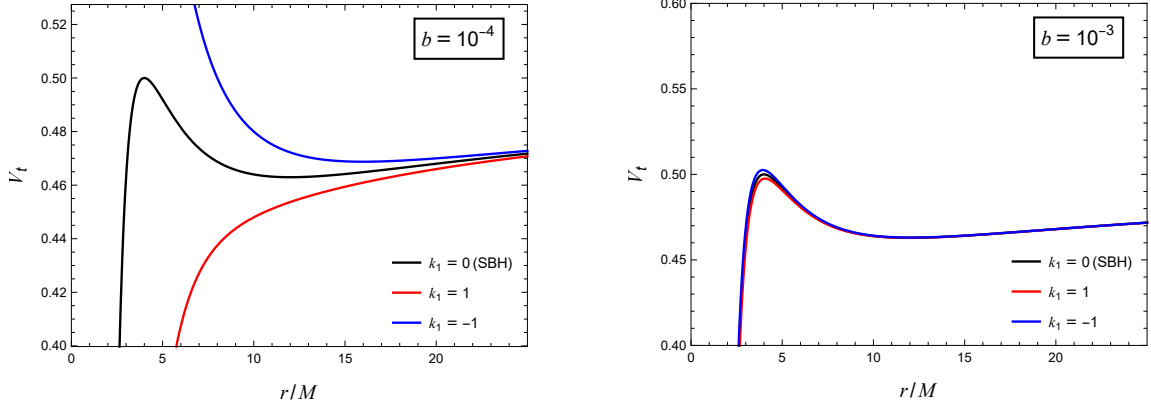


FIG. 3: Effective potential $V_t(r)$ for massive particles with $G = 1$, $\ell_P/R_S = 10^{-4}$, $L = 4M$, and different values of k_1 (see Eq. (46) with $\alpha = 1$). The black lines refer to the classical Schwarzschild black hole, abbreviated as “SBH”, where V_t admits a maximum at $r = 4M$ and a minimum at $r = 12M$. In the left panel, V_t has no extremum when $k_1 = 1$, while for $k_1 = -1$ it reaches the minimum at $r = 16M$. In the right panel, V_t exhibits a maximum at $r = 4.06M$ and a minimum at $r = 11.94M$ for $k_1 = 1$, while for $k_1 = -1$ these extrema are achieved at $r = 3.94M$ and $r = 12.06M$, respectively.

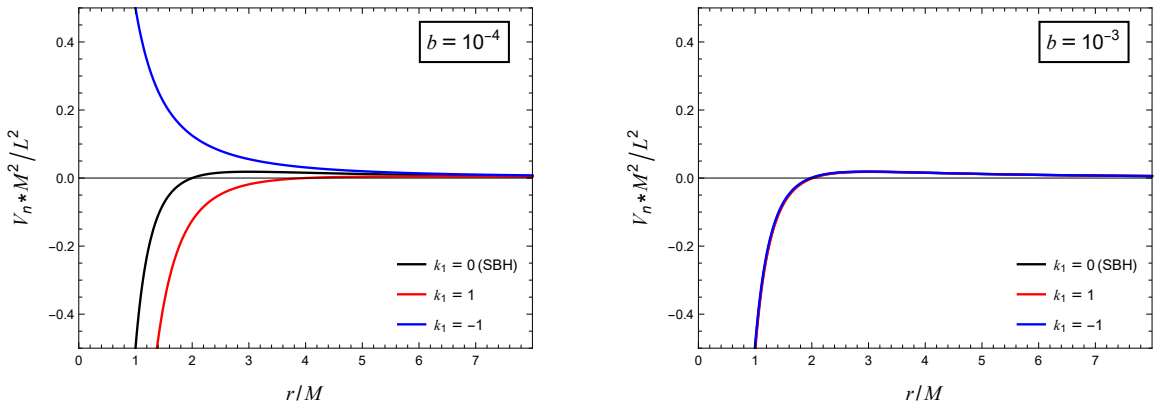


FIG. 4: Effective potential $V_n(r)$ for massless particles with $G = 1$, $\ell_P/R_S = 10^{-4}$, and $k_1 = 0, \pm 1$ (see Eq. (46) with $\alpha = 0$). For the classical Schwarzschild black hole (SBH), V_n attains its maximum value at the b -independent point $r = 3M$. In the left panel, V_n admits no maximum when $k_1 = -1$, while for $k_1 = 1$ it is reached at $r = 6M$, which does not correspond to the photon sphere radius due to the energy dependence in the effective potential (a more detailed discussion will be provided in Sec. III C). In the right panel, the quantum and classical effective potentials almost overlap, with the maximum of V_n occurring at $r = 3.03M$ for $k_1 = 1$ and $r = 2.97M$ for $k_1 = -1$.

either A or B , or both, are zero (the first situation occurs at the metric horizons r_i , with $i = 1, 2, 3$, where $B(r_i) = 0$ and $A(r_i) \neq 0$). This feature cannot be inferred from the expressions (45) and (46), as their derivation relies only on one-loop quantities stemming from A^{-1} and $(AB)^{-1}$. If we had an *exact* formula for both A and B , then the analysis of

the geodesic motion would have required the use of Eq. (44), rather than Eqs. (45) and (46). However, an exact form of A and B can only be obtained via a full-loop calculation, which makes sense in a fully quantum regime. In this framework, the geodesic equation does not give a reliable description of the dynamics of a freely falling particle² and hence one should resort to quantum-mechanics tools, which we expect not to be plagued by the presence of an infinite-depth barrier. However, since in this paper we only deal with the first low-energy quantum modifications of the classical Schwarzschild solution, a first approach where general-relativity techniques are employed for the study of the dynamics is reasonable.

We begin our investigation with timelike geodesics. In Sec. III A, we show that in the quantum realm the positions of stable and unstable circular orbits are described by a quartic algebraic equation, for which we propose an analytic method to find its roots; as we will see, the solutions are written in an approximated form which is consistent with the EFT recipes and the ensuing constraint (3). After that, massive bodies trajectories are considered in Sec. III B. Finally, we delve into null geodesics in Sec. III C, where we first exploit the aforementioned analytic technique to work out the quantum corrected photon sphere radii, and then examine the motion of photons. Our analysis unveils that the effect of the quantum contributions on the orbits of both massive and massless particles can give rise to intriguing phenomena.

A. Timelike geodesics: stable and unstable circular orbits

A first preliminary study of stable and unstable circular orbits and, in particular, of the quantum corrections to the innermost stable circular orbit (ISCO) radius, has been given in Ref. [93]. In this section, we extend this former examination by providing an analytic method for obtaining in a straightforward way the quantum corrected radii of such trajectories for both positive and negative k_1 scenarios.

The analysis of timelike geodesics can be performed via Eq. (45), where the effective potential should be evaluated by setting $\alpha = 1$. In this way, from Eq. (46) we obtain the

² See e.g. Refs. [115–118], where it is suggested that at quantum level some classical formulations of the equivalence principle seem to be violated.

“timelike potential” (see Fig. 3)

$$V_t(r) = \frac{1}{2} \left(1 - \frac{R_S}{r}\right) \left(\frac{L^2}{r^2} + 1\right) + \frac{1}{2} k_1 \left(\frac{3}{2} - \mathcal{E}^2\right) \frac{R_S \ell_P^2}{r^3}, \quad (47)$$

whose first-order and second-order derivatives with respect to the radial variable (denoted with a prime) read as

$$V_t'(r) = \frac{1}{r^4} \left[\frac{r^2 R_S}{2} + L^2 \left(\frac{3}{2} R_S - r\right) + \frac{9}{4} k_1 R_S \ell_P^2 \left(\frac{2}{3} \mathcal{E}^2 - 1\right) \right], \quad (48a)$$

$$V_t''(r) = \frac{1}{r^5} \left[3L^2(r - 2R_S) - R_S r^2 - 9k_1 R_S \ell_P^2 \left(\frac{2}{3} \mathcal{E}^2 - 1\right) \right], \quad (48b)$$

respectively. Let $E := \mathcal{E}(\mathcal{R})$ denote the value of the energy (per unit rest mass) of a particle following a circular orbit of radius \mathcal{R} , where \mathcal{R} represents one of the extrema of $V_t(r)$, which thus satisfies $V_t'(\mathcal{R}) = 0$. From the well-known relation $(1/2)E^2 = V_t(\mathcal{R})$ (cf. Eq. (45)), we find modulo $O(\mathcal{R}^{-4})$ contributions

$$E^2 = 1 - \frac{R_S}{\mathcal{R}} + \frac{L^2}{\mathcal{R}^2} - \frac{L^2 R_S}{\mathcal{R}^3} + \frac{k_1 R_S \ell_P^2}{2 \mathcal{R}^3}. \quad (49)$$

We can further simplify this equation by exploiting the condition $V_t'(\mathcal{R}) = 0$, which gives an expression for the ratio L^2/\mathcal{R}^2 . In this way, by neglecting higher-order terms, we obtain from Eq. (49) the following formula pertaining to the quantum corrected energy:

$$E = \left[\frac{2(\mathcal{R} - R_S)^2}{\mathcal{R}(2\mathcal{R} - 3R_S)} + (k_1 R_S \ell_P^2) \frac{12(\mathcal{R} - R_S)^3 + \mathcal{R}(6R_S - 7\mathcal{R})(2\mathcal{R} - 3R_S)}{2\mathcal{R}^4(2\mathcal{R} - 3R_S)^2} \right]^{1/2}. \quad (50)$$

By means of Eq. (49), the relation $V_t'(\mathcal{R}) = 0$ gives the fifth-order algebraic equation

$$(R_S) \mathcal{R}^5 - (2L^2) \mathcal{R}^4 + (3R_S L^2) \mathcal{R}^3 + \frac{3}{2} k_1 R_S \ell_P^2 [-\mathcal{R}^3 - (2R_S) \mathcal{R}^2 + (2L^2) \mathcal{R} - 2L^2 R_S + k_1 R_S \ell_P^2] = 0. \quad (51)$$

Quintic equations are characterized by a rich mathematical theory. The Abel-Ruffini theorem asserts that the solutions of the equations of degree five or higher over the rationals cannot be given in terms of radicals, and hence more involved functions will occur in their

resolution process. An example is furnished by the Birkeland algorithm, which expresses the roots of any quintic via generalized hypergeometric functions. Such procedure can be employed with notable success once the quintic has been brought to so called Bring-Jerrard form, i.e., it can be written as $X^5 + aX + d = 0$. This reduction can always be done by introducing a polynomial transformation known as Tschirnhaus transformation, which is defined in such a way as to remove the factors of degree four, three, and two from the quintic. Another notable method to address fifth-order equations is due to Hermite, who has proved that a quintic in the Bring-Jerrard form can be solved by means of elliptic functions. Moreover, more recently a valuable technique has been set forth in Ref. [119], where it is shown how the roots of the quintic can be represented through the Jacobi nome and the theta series. For further details regarding fifth-degree equations and their applications in quantum settings we refer the reader to Refs. [21, 35] and references therein.

It is thus clear that the resolution of the quintic (51) inevitably involves special functions. Therefore, attempting to decrease its degree can provide substantial advantages. Remarkably, this reduction can be achieved within our model. Indeed, if we use Eq. (49) to express L^2 in terms of E^2 and \mathcal{R} , we obtain

$$L^2 = \frac{\mathcal{R}^3 E^2 - k_1 R_S \ell_P^2 / 2}{\mathcal{R} - R_S} - \mathcal{R}^2, \quad (52)$$

with which we can write the condition $V_t'(\mathcal{R}) = 0$ as the following quartic equation:

$$\begin{aligned} (1 - E^2) \mathcal{R}^4 + R_S \left(\frac{3}{2} E^2 - 2 \right) \mathcal{R}^3 + R_S^2 \mathcal{R}^2 + \frac{1}{2} k_1 R_S \ell_P^2 \left(3E^2 - \frac{7}{2} \right) \mathcal{R} \\ + \frac{3}{2} k_1 R_S^2 \ell_P^2 (1 - E^2) = 0. \end{aligned} \quad (53)$$

The physically meaningful solutions of this equation are the positive real-valued radii giving positive values of E and L^2 (see Eqs. (49), (50), and (52)). Stable circular orbits (SCOs) having radius \mathcal{R} are singled out by relation $V_t''(\mathcal{R}) \geq 0$ (cf. Eq. (48b)), where we will show that, similarly to the classical Schwarzschild framework, the equal sign is attained at the ISCO; on the other hand, for unstable circular orbits (UCOs) the condition $V_t''(\mathcal{R}) < 0$ holds. We first solve the quartic (53) in the classical case in Sec. III A 1, which prepares the ground for the investigation in the quantum realm, to be performed in Sec. III A 2.

1. *Analysis of the quartic equation in the classical regime*

In the classical regime $k_1 = 0$, the quartic (53), which, as pointed out before, governs the position of both SCOs and UCOs, boils down to a second-order equation. In order to make contact with the notations to be introduced in Sec. III A 2, we write the ensuing roots in the following way:

$$\bar{\mathcal{R}}_3 = \frac{(3\bar{E}^2 - 4 + \bar{E}\sqrt{9\bar{E}^2 - 8}) R_S}{4(\bar{E}^2 - 1)}, \quad (54a)$$

$$\bar{\mathcal{R}}_4 = \frac{(3\bar{E}^2 - 4 - \bar{E}\sqrt{9\bar{E}^2 - 8}) R_S}{4(\bar{E}^2 - 1)}, \quad (54b)$$

where \bar{E} is the classical energy which can be read off from Eq. (50) with $k_1 = 0$. It is simple to show [106] that, when $L^2 > 12M^2$, $\bar{\mathcal{R}}_3$ is the maximum while $\bar{\mathcal{R}}_4$ the minimum of the classical effective potential, which can be readily deduced from Eq. (47). While $\bar{\mathcal{R}}_4$ is defined only if $\bar{E}^2 \neq 1$, $\bar{\mathcal{R}}_3$ admits a continuous extension at $\bar{E} = 1$, where it attains the value

$$\bar{\mathcal{R}}_3^{(\bar{E}=1)} =: \bar{\mathcal{R}}_+ = 2R_S, \quad (55)$$

which can be easily obtained also from the quartic (53) in the limit $k_1 = 0$ and $E^2 \equiv \bar{E}^2 = 1$.

The plots of $\bar{\mathcal{R}}_3$ and $\bar{\mathcal{R}}_4$ are displayed in Figs. 5 and 6, respectively, where the following

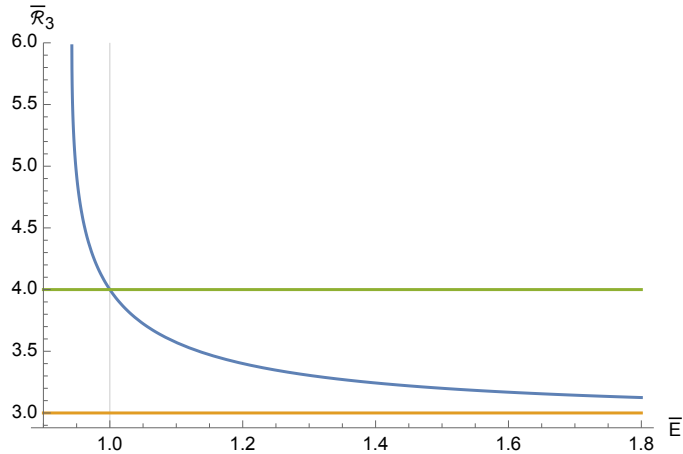


FIG. 5: The solution $\bar{\mathcal{R}}_3$ as a function of \bar{E} with $M = G = 1$ (see Eq. (54a)). It is clear that $\bar{\mathcal{R}}_3$ lies between $3M$ and $6M$ and that \bar{E}^2 becomes smaller than one as soon as $\bar{\mathcal{R}}_3 > 4M$. Moreover, $\bar{\mathcal{R}}_3$ admits a continuous extension at $\bar{E} = 1$, as reported in Eq. (55).

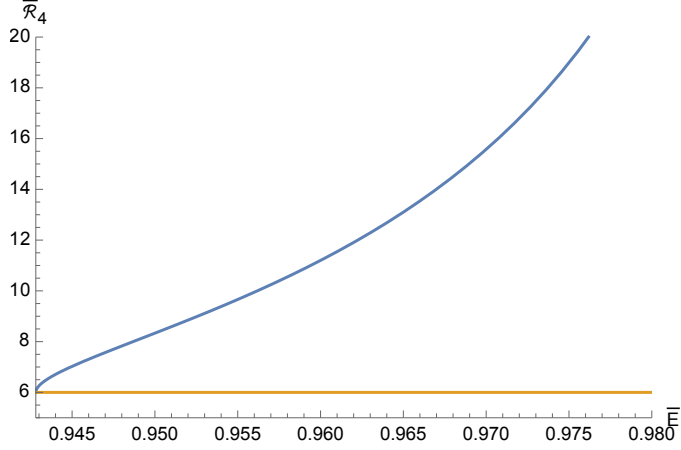


FIG. 6: The solution $\bar{\mathcal{R}}_4$ as a function of \bar{E} with $M = G = 1$ (see Eq. (54b)). It is evident that $\bar{\mathcal{R}}_4 \geq 6M$ and $8/9 \leq \bar{E}^2 < 1$.

well-known classical results are evident [106, 120]:

$$\frac{3}{2}R_S < \bar{\mathcal{R}}_3 \leq 3R_S, \quad (56a)$$

$$\bar{\mathcal{R}}_4 \geq 3R_S, \quad (56b)$$

$$\frac{8}{9} \leq \bar{E}^2 < 1, \quad \text{if } \bar{\mathcal{R}} > 2R_S, \quad (56c)$$

$$\bar{E}^2 \geq 1, \quad \text{if } \frac{3}{2}R_S < \bar{\mathcal{R}}_3 \leq 2R_S, \quad (56d)$$

where in Eq. (56c) $\bar{\mathcal{R}}$ denotes either $\bar{\mathcal{R}}_3$ or $\bar{\mathcal{R}}_4$. The lower bound $\bar{E}^2 \geq 8/9$ guarantees that $\bar{\mathcal{R}}_{3,4}$ are well-defined functions; in particular, $\bar{\mathcal{R}}_3$ attains its minimum value when $\bar{E} \gg 1$, as

$$\lim_{\bar{E} \rightarrow +\infty} \bar{\mathcal{R}}_3 = \frac{3}{2}R_S; \quad (57)$$

moreover, SCOs with radius $\bar{\mathcal{R}}_4$ have always $8/9 \leq \bar{E}^2 < 1$; lastly, when

$$\bar{E}^2 = 8/9 =: \bar{E}_{\text{ISCO}}^2, \quad (58)$$

then $\bar{\mathcal{R}}_3$ and $\bar{\mathcal{R}}_4$ coincide and yield the classical ISCO radius

$$\bar{\mathcal{R}}_{\text{ISCO}} = 3R_S. \quad (59)$$

2. *Analysis of the quartic equation in the quantum regime*

We are now ready to address the resolution of Eq. (53) in the quantum scenario, where $k_1 \neq 0$.

Let us first consider the case $E^2 = 1$. In this hypothesis, the quartic (53) reduces to the quadratic equation

$$\mathcal{R}^2 R_S - 2R_S^2 \mathcal{R} + \frac{1}{2} k_1 R_S \ell_P^2 = 0, \quad (60)$$

which gives the exact solutions

$$\mathcal{R}_\pm = R_S \pm \frac{1}{2} \sqrt{4R_S^2 - 2k_1 \ell_P^2}. \quad (61)$$

The corresponding values of the angular momentum follow from Eq. (52) and read as

$$L_\pm^2 = R_S \left(2R_S \pm \sqrt{4R_S^2 - 2k_1 \ell_P^2} \right), \quad (62)$$

while thanks to Eq. (48b) we obtain

$$V_t''(\mathcal{R}_\pm) = -\frac{8R_S \left[R_S \left(\sqrt{4R_S^2 - 2k_1 \ell_P^2} \pm 2R_S \right) \mp k_1 \ell_P^2 \right]}{\sqrt{R_S^2 - \frac{k_1 \ell_P^2}{2}} \left(\sqrt{4R_S^2 - 2k_1 \ell_P^2} \pm 2R_S \right)^4}. \quad (63)$$

It should be noted that the radii \mathcal{R}_\pm correspond to *different* envelopes of the effective potential as they are characterized by distinct L^2 .

If we exploit the approximation (3), which is valid within the EFT paradigm, then from Eq. (61) we can write

$$\mathcal{R}_+ = 2R_S - (k_1/4)(\ell_P^2/R_S) + O(\ell_P^4/R_S^3), \quad (64)$$

$$\mathcal{R}_- = (k_1/4)(\ell_P^2/R_S) + O(\ell_P^4/R_S^3), \quad (65)$$

the solution (64) being in agreement with the classical result (55) in the limit $k_1 = 0$; moreover, upon discarding higher-order corrections and recalling the condition (2), Eq. (63)

yields

$$V_t''(\mathcal{R}_+) = -\frac{64R_S^6(8R_S^2 - 3k_1\ell_P^2)}{(k_1\ell_P^2 - 8R_S^2)^4(4R_S^2 - k_1\ell_P^2)} < 0, \quad (66)$$

$$V_t''(\mathcal{R}_-) = -\frac{64R_S^6}{k_1^3\ell_P^6(4R_S^2 - k_1\ell_P^2)}. \quad (67)$$

From the preceding equations, it is evident that in our hypotheses both \mathcal{R}_+ and L_+^2 remain positive regardless of the sign assumed by k_1 , with the former being the maximum of the effective potential. This is not true for \mathcal{R}_- and L_-^2 . In fact, they are both negative, and hence nonphysical, when k_1 is negative. For $k_1 > 0$, \mathcal{R}_- is positive and represents the maximum of the effective potential, since $V_t''(\mathcal{R}_-) < 0$. Therefore, we can conclude that no SCO exists when $E^2 = 1$. This situation reflects the classical scenario, where the value $\bar{E}^2 = 1$ gives the root $\bar{\mathcal{R}}_+ = 2R_S$ (cf. Eq. (55)), which corresponds to a radius falling within the range of UCOs (see Eq. (56a)).

At this stage, we can examine the general case with $E^2 \neq 1$. With this assumption, Eq. (53) can be expressed in the standard quartic form:

$$\mathcal{R}^4 + a_3\mathcal{R}^3 + a_2\mathcal{R}^2 + a_1\mathcal{R} + a_0 = 0, \quad (68a)$$

with

$$\begin{aligned} a_3 &= \frac{(3E^2/2 - 2)R_S}{1 - E^2}, \\ a_2 &= \frac{R_S^2}{1 - E^2}, \\ a_1 &= \frac{(3E^2 - 7/2)k_1\ell_P^2R_S}{2(1 - E^2)}, \\ a_0 &= \frac{3k_1\ell_P^2R_S^2}{2}. \end{aligned} \quad (68b)$$

In the literature, there exist various methodologies to solve a quartic exactly [121]. However, these approaches usually envisage a long procedure and the ensuing roots involve lengthy expressions. For this reason, we now propose a simple analytical technique for finding the approximated form of the solutions of the quartic (68), which thus assume a readable and ready-to-use form. Following the principles of the EFT scheme, we suppose that the roots of Eq. (68) can be expanded as power series in $(\ell_P/R_S)^n$, where the leading-order term is represented by the classical solution and n is a positive real number to be determined

shortly. Accordingly, we have

$$\mathcal{R}_1 = \bar{\mathcal{R}}_1 + f_1 (\ell_P/R_S)^n + f_2 (\ell_P/R_S)^{2n} + O(\ell_P/R_S)^{3n}, \quad (69a)$$

$$\mathcal{R}_2 = \bar{\mathcal{R}}_2 + f_3 (\ell_P/R_S)^n + f_4 (\ell_P/R_S)^{2n} + O(\ell_P/R_S)^{3n}, \quad (69b)$$

$$\mathcal{R}_3 = \bar{\mathcal{R}}_3 + f_5 (\ell_P/R_S)^n + f_6 (\ell_P/R_S)^{2n} + O(\ell_P/R_S)^{3n}, \quad (69c)$$

$$\mathcal{R}_4 = \bar{\mathcal{R}}_4 + f_7 (\ell_P/R_S)^n + f_8 (\ell_P/R_S)^{2n} + O(\ell_P/R_S)^{3n}, \quad (69d)$$

with $\bar{\mathcal{R}}_1 = \bar{\mathcal{R}}_2 = 0$ (i.e., \mathcal{R}_1 and \mathcal{R}_2 are fully quantum radii), while $\bar{\mathcal{R}}_3$ and $\bar{\mathcal{R}}_4$ are given in Eq. (54). Bearing in mind the coefficients (68b), a self-consistent perturbative solution of the quartic can be achieved when $n = 1$. Then, the factors f_i can be determined by substituting \mathcal{R}_i back into Eq. (68). For example, by plugging \mathcal{R}_1 into Eq. (68), we have

$$\begin{aligned} & \left(\frac{f_1^2}{1-E^2} + \frac{3k_1 R_S^2}{2} \right) \ell_P^2 + \left[f_1 \frac{(8-6E^2) f_1^2/R_S^2 + (7-6E^2) k_1 - 8f_2/R_S}{4(E^2-1)} \right] \ell_P^3 \\ & + O(\ell_P^4) = 0. \end{aligned} \quad (70)$$

This equation requires that the terms proportional to ℓ_P^2 and ℓ_P^3 be zero separately, i.e.,

$$0 = \frac{f_1^2}{1-E^2} + \frac{3k_1 R_S^2}{2}, \quad (71)$$

$$0 = \frac{f_1 [(8-6E^2) f_1^2/R_S^2 + (7-6E^2) k_1 - 8f_2/R_S]}{4(E^2-1)}, \quad (72)$$

which yield

$$f_1 = \pm \sqrt{\frac{3k_1}{2}(E^2-1)} R_S, \quad (73)$$

$$f_2 = \frac{-9E^4 + 15E^2 - 5}{8} k_1 R_S. \quad (74)$$

Similarly, considering \mathcal{R}_2 we obtain

$$f_3 = \pm \sqrt{\frac{3k_1}{2}(E^2-1)} R_S, \quad (75)$$

$$f_4 = f_2. \quad (76)$$

To be specific, in order to let \mathcal{R}_1 and \mathcal{R}_2 represent distinct solutions, we choose different

values for f_1 and f_3 , i.e.,

$$f_1 = -f_3 = \sqrt{\frac{3k_1}{2}(E^2 - 1)} R_S, \quad (77)$$

which means that \mathcal{R}_1 and \mathcal{R}_2 take the form

$$\mathcal{R}_1 = \sqrt{\frac{3k_1}{2}(E^2 - 1)} \ell_P - \left(\frac{9E^4 - 15E^2 + 5}{8} \right) k_1 \ell_P^2 / R_S + O(\ell_P^3 / R_S^2), \quad (78a)$$

$$\mathcal{R}_2 = -\sqrt{\frac{3k_1}{2}(E^2 - 1)} \ell_P - \left(\frac{9E^4 - 15E^2 + 5}{8} \right) k_1 \ell_P^2 / R_S + O(\ell_P^3 / R_S^2). \quad (78b)$$

By employing the same method, we obtain the other two roots \mathcal{R}_3 and \mathcal{R}_4 for the quartic equation.

For $E^2 \neq 8/9$, these are given by

$$\begin{aligned} \mathcal{R}_3^{\text{case1}} &= \bar{\mathcal{R}}_3 + \left[\frac{9E^4 - 15E^2 + 5}{8} - \frac{(27E^6 - 57E^4 + 27E^2 + 4)}{8E\sqrt{9E^2 - 8}} \right] k_1 \ell_P^2 / R_S \\ &+ O(\ell_P^3 / R_S^2), \end{aligned} \quad (78c)$$

$$\begin{aligned} \mathcal{R}_4^{\text{case1}} &= \bar{\mathcal{R}}_4 + \left[\frac{9E^4 - 15E^2 + 5}{8} + \frac{(27E^6 - 57E^4 + 27E^2 + 4)}{8E\sqrt{9E^2 - 8}} \right] k_1 \ell_P^2 / R_S \\ &+ O(\ell_P^3 / R_S^2), \end{aligned} \quad (78d)$$

while for $E^2 = 8/9$, we have

$$\mathcal{R}_3^{\text{case2}} = 3R_S - \frac{1}{2} \sqrt{\frac{13k_1}{3}} \ell_P - \left(\frac{11k_1}{72} \right) \ell_P^2 / R_S + O(\ell_P^3 / R_S^2), \quad (78e)$$

$$\mathcal{R}_4^{\text{case2}} = 3R_S + \frac{1}{2} \sqrt{\frac{13k_1}{3}} \ell_P - \left(\frac{11k_1}{72} \right) \ell_P^2 / R_S + O(\ell_P^3 / R_S^2). \quad (78f)$$

It is possible to unify these two sets of solutions into a single one, yielding

$$\begin{aligned} \mathcal{R}_3 &= \frac{R_S}{4(E^2 - 1)} \sqrt{E^2(9E^2 - 8) + (4 - 27E^8 + 84E^6 - 84E^4 + 23E^2)k_1 \ell_P^2 / R_S^2} \\ &+ \frac{(3E^2 - 4)R_S}{4(E^2 - 1)} + \frac{(9E^4 - 15E^2 + 5)k_1 \ell_P^2}{8R_S} + O(\ell_P^3 / R_S^2), \end{aligned} \quad (79)$$

$$\begin{aligned} \mathcal{R}_4 &= -\frac{R_S}{4(E^2 - 1)} \sqrt{E^2(9E^2 - 8) + (4 - 27E^8 + 84E^6 - 84E^4 + 23E^2)k_1 \ell_P^2 / R_S^2} \\ &+ \frac{(3E^2 - 4)R_S}{4(E^2 - 1)} + \frac{(9E^4 - 15E^2 + 5)k_1 \ell_P^2}{8R_S} + O(\ell_P^3 / R_S^2). \end{aligned} \quad (80)$$

It is easy to check that the analytic solutions (78)–(80) provided by our approach are

$$k_1 = 1, E = 10, \ell_P/R_S = 10^{-4}$$

Solution	\mathcal{R}_1/R_S	\mathcal{R}_2/R_S	\mathcal{R}_3/R_S	\mathcal{R}_4/R_S
Analytic solution	0.00111	-0.00133	1.50168	-0.00651
Numerical solution	0.00111	-0.00137	1.50168	-0.00649
$V_t''(\mathcal{R}_i)R_S^2$	6.05177×10^8	-3.59837×10^8	-132.001	-3.59127×10^6
Sign of L^2	-	-	+	-

$$k_1 = 1, E = 2, \ell_P/R_S = 10^{-4}$$

Solution	\mathcal{R}_1/R_S	\mathcal{R}_2/R_S	\mathcal{R}_3/R_S	\mathcal{R}_4/R_S
Analytic solution	0.00021	-0.00021	1.54858	-0.21525
Numerical solution	0.00021	-0.00021	1.54858	-0.21525
$V_t''(\mathcal{R}_i)R_S^2$	1.04941×10^{11}	-1.04572×10^{11}	-4.02223	-93.9781
Sign of L^2	-	-	+	-

$$k_1 = 1, E = 1.01, \ell_P/R_S = 10^{-4}$$

Solution	\mathcal{R}_1/R_S	\mathcal{R}_2/R_S	\mathcal{R}_3/R_S	\mathcal{R}_4/R_S
Analytic solution	0.00002	-0.00002	1.96342	-25.33900
Numerical solution	0.00002	-0.00002	1.96342	-25.33900
$V_t''(\mathcal{R}_i)R_S^2$	1.90925×10^{14}	-1.91106×10^{14}	-0.741159	-0.00032
Sign of L^2	+	+	+	-

$$k_1 = 1, E = 0.99, \ell_P/R_S = 10^{-4}$$

Solution	\mathcal{R}_1/R_S	\mathcal{R}_2/R_S	\mathcal{R}_3/R_S	\mathcal{R}_4/R_S
Analytic solution	0.00002i	-0.00002i	2.04428	24.58130
Numerical solution	0.00002i	-0.00002i	2.04428	24.58130
$V_t''(\mathcal{R}_i)R_S^2$	Complex	Complex	-0.10277	0.00003
Sign of L^2	Complex	Complex	+	+

$$k_1 = 1, E = \sqrt{8/9}, \ell_P/R_S = 10^{-4}$$

Solution	\mathcal{R}_1/R_S	\mathcal{R}_2/R_S	\mathcal{R}_3/R_S	\mathcal{R}_4/R_S
Analytic solution	0.00004i	-0.00004i	2.99990	3.00010
Numerical solution	0.00004i	-0.00004i	2.99990	3.00010
$V_t''(\mathcal{R}_i)R_S^2$	Complex	Complex	-1.28515×10^{-6}	1.28481×10^{-6}
Sign of L^2	Complex	Complex	+	+

$$k_1 = 1, E = 0.5, \ell_P/R_S = 10^{-4}$$

Solution	\mathcal{R}_1/R_S	\mathcal{R}_2/R_S	\mathcal{R}_3/R_S	\mathcal{R}_4/R_S
Analytic solution	0.00011i	-0.00011i	1.08333-0.39965i	1.08333-0.39965i
Numerical solution	0.00011i	-0.00011i	1.08333-0.39965i	1.08333-0.39965i
$V_t''(\mathcal{R}_i)R_S^2$	Complex	Complex	Complex	Complex
Sign of L^2	Complex	Complex	Complex	Complex

TABLE I: Roots (in units of R_S) of the quartic (68) obtained analytically via our method and numerically for $k_1 = 1$ and various choices of the energy E ; the values of $V_t''(\mathcal{R}_i)$ and L^2 , which follow from Eqs. (48b) and (52), respectively, are also provided. The agreement between our approach and the numerics is evident.

$$k_1 = -1, E = 10, \ell_P/R_S = 10^{-4}$$

Solution	\mathcal{R}_1/R_S	\mathcal{R}_2/R_S	\mathcal{R}_3/R_S	\mathcal{R}_4/R_S
Analytic solution	0.00011+0.00122i	0.00011-0.00122i	1.50168	-0.00695
Numerical solution	0.00010+0.00120i	0.00010-0.00120i	1.50168	-0.00693
$V_t''(\mathcal{R}_i)R_S^2$	Complex	Complex	-132.001	-2.95082×10^6
Sign of L^2	Complex	Complex	+	-

$$k_1 = -1, E = 2, \ell_P/R_S = 10^{-4}$$

Solution	\mathcal{R}_1/R_S	\mathcal{R}_2/R_S	\mathcal{R}_3/R_S	\mathcal{R}_4/R_S
Analytic solution	0.00021i	-0.00021i	1.54858	-0.21525
Numerical solution	0.00021i	-0.00021i	1.54858	-0.21525
$V_t''(\mathcal{R}_i)R_S^2$	Complex	Complex	-4.02223	-93.9775
Sign of L^2	Complex	Complex	+	-

$$k_1 = -1, E = 1.01, \ell_P/R_S = 10^{-4}$$

Solution	\mathcal{R}_1/R_S	\mathcal{R}_2/R_S	\mathcal{R}_3/R_S	\mathcal{R}_4/R_S
Analytic solution	0.00002i	-0.00002i	1.96342	-25.33900
Numerical solution	0.00002i	-0.00002i	1.96342	-25.33900
$V_t''(\mathcal{R}_i)R_S^2$	Complex	Complex	-0.147759	-0.00003
Sign of L^2	Complex	Complex	+	-

$$k_1 = -1, E = 0.99, \ell_P/R_S = 10^{-4}$$

Solution	\mathcal{R}_1/R_S	\mathcal{R}_2/R_S	\mathcal{R}_3/R_S	\mathcal{R}_4/R_S
Analytic solution	0.00002	-0.00002	2.04428	24.58130
Numerical solution	0.00002	-0.00002	2.04428	24.58130
$V_t''(\mathcal{R}_i)R_S^2$	1.94006×10^{14}	-1.93799×10^{14}	-0.102766	0.00003
Sign of L^2	-	-	+	+

$$k_1 = -1, E = \sqrt{8/9} + 0.00001, \ell_P/R_S = 10^{-4}$$

Solution	\mathcal{R}_1/R_S	\mathcal{R}_2/R_S	\mathcal{R}_3/R_S	\mathcal{R}_4/R_S
Analytic solution	0.00004	-0.00004	2.97274	3.02802
Numerical solution	0.00004	-0.00004	2.97274	3.02802
$V_t''(\mathcal{R}_i)R_S^2$	1.47047×10^{13}	-1.46966×10^{13}	-0.00035	0.00033
Sign of L^2	-	-	+	+

$$k_1 = -1, E = \sqrt{8/9}, \ell_P/R_S = 10^{-4}$$

Solution	\mathcal{R}_1/R_S	\mathcal{R}_2/R_S	\mathcal{R}_3/R_S	\mathcal{R}_4/R_S
Analytic solution	0.00004	-0.00004	3-0.00010i	3+0.00010i
Numerical solution	0.00004	-0.00004	3-0.00010i	3+0.00010i
$V_t''(\mathcal{R}_i)R_S^2$	1.47010×10^{13}	-1.46929×10^{13}	Complex	Complex
Sign of L^2	-	-	Complex	Complex

$$k_1 = -1, E = 0.5, \ell_P/R_S = 10^{-4}$$

Solution	\mathcal{R}_1/R_S	\mathcal{R}_2/R_S	\mathcal{R}_3/R_S	\mathcal{R}_4/R_S
Analytic solution	0.00011	-0.00011	1.08333-0.39965i	1.08333-0.39965i
Numerical solution	0.00011	-0.00011	1.08333-0.39965i	1.08333-0.39965i
$V_t''(\mathcal{R}_i)R_S^2$	8.38127×10^{11}	-8.37978×10^{11}	Complex	Complex
Sign of L^2	-	-	Complex	Complex

TABLE II: Roots (in units of R_S) of the quartic (68) for $k_1 = -1$ and different values of E . Our analytical method and the numerical approach agree with high accuracy.

such that the Viète formulas for quartic equations [121] are satisfied modulo higher-order terms in ℓ_{P} , as we obtain

$$\sum_{i=1}^4 \mathcal{R}_i = -a_3 + O(\ell_{\text{P}}^3/R_{\text{S}}^2), \quad (81\text{a})$$

$$\sum_{i,j=1}^4 \mathcal{R}_i \mathcal{R}_j = a_2 + O(\ell_{\text{P}}^4/R_{\text{S}}^2), \quad \text{for } i \neq j, \quad (81\text{b})$$

$$\sum_{i,j,k=1}^4 \mathcal{R}_i \mathcal{R}_j \mathcal{R}_k = -a_1 + O(\ell_{\text{P}}^4/R_{\text{S}}), \quad \text{for } i \neq j \neq k, \quad (81\text{c})$$

$$\mathcal{R}_1 \mathcal{R}_2 \mathcal{R}_3 \mathcal{R}_4 = a_0 + O(\ell_{\text{P}}^4). \quad (81\text{d})$$

Moreover, we find that our formulas align closely with the numerical solutions, as evidenced in Tables I and II. As can be inferred from the values of $V_t''(\mathcal{R}_i)$ ($i = 1, 2, 3, 4$) reported in the tables, we have also verified that \mathcal{R}_3 is the maximum while \mathcal{R}_4 the minimum of the effective potential when $E_{\text{ISCO}}^2 < E^2 < 1$, where the quantum ISCO energy E_{ISCO}^2 will be derived in Eq. (88) below.

It is worth noticing that, although the solutions (78)–(80) have been derived by supposing $E \neq 1$, some of them admit a continuous extension when $E = 1$. Indeed, up to higher-order corrections, we have that $\mathcal{R}_1^{(E=1)} + \mathcal{R}_2^{(E=1)} = \mathcal{R}_-$, and $\mathcal{R}_3^{(E=1)} = \mathcal{R}_+$ like in the classical case (see Eq. (55)); on the other hand, \mathcal{R}_4 cannot be extended at $E = 1$, since its classical piece $\bar{\mathcal{R}}_4$ is not defined in this limit.

At this stage, some remarks should be made. Following EFT principles, quantum contributions to a physical quantity should not become more important than the classical ones. Since quantum terms in \mathcal{R}_i ($i = 1, 2, 3, 4$) depend on E , some constraints on this constant should be taken into account. While mathematically there may be no upper bound on E , physically the energy cannot be arbitrarily large, otherwise one can no longer neglect the particle back-reaction on the geometry. This is true also in our model, as $\mathcal{R}_{3,4}$ appear in the form of a classical piece $\bar{\mathcal{R}}_{3,4}$ plus a tiny quantum factor, if

$$E \ll R_{\text{S}}/\ell_{\text{P}}, \quad (82)$$

or, equivalently,

$$E \ll M/M_{\text{P}}, \quad (83)$$

which prevent the energy from attaining huge values in view of Eqs. (3) and (4). Therefore, the above equations suggest that $R_{\text{S}}/\ell_{\text{P}}$, or equivalently M/M_{P} , can be interpreted as a cutoff energy scale of our model.

In the classical scenario with $k_1 = 0$, the attainment of the ISCO occurs precisely when $\bar{E}_{\text{ISCO}}^2 = 8/9$ (cf. Eq. (58)). The classical ISCO radius can be determined by equating Eq. (78e) to Eq. (78f) in the limit $k_1 = 0$, which indeed yields the value (59). This criterion is no longer sustained in the quantum realm, as Eq. (78e) differs from Eq. (78f) for $k_1 \neq 0$. For this reason, we first find the ISCO energy by equating Eq. (79) to Eq. (80), which gives

$$E^2 (9E^2 - 8) R_{\text{S}}^2 + (-27E^8 + 84E^6 - 84E^4 + 23E^2 + 4) k_1 \ell_{\text{P}}^2 = 0. \quad (84)$$

Not all of the roots of Eq. (84) are physically relevant, since we are interested in the solution which slightly deviates from the corresponding classical one. Therefore, we exploit again our method and assume that E_{ISCO}^2 admits the expansion

$$E_{\text{ISCO}}^2 = \bar{E}_{\text{ISCO}}^2 + f_9 (\ell_{\text{P}}/R_{\text{S}}) + f_{10} (\ell_{\text{P}}^2/R_{\text{S}}^2) + \text{O}(\ell_{\text{P}}^3/R_{\text{S}}^3), \quad (85)$$

where the classical value \bar{E}_{ISCO}^2 has been given in Eq. (58). Upon substituting the above expression back into Eq. (84) and imposing the condition that terms proportional to ℓ_{P} and ℓ_{P}^2 vanish independently, we obtain

$$f_9 = 0, \quad (86)$$

$$f_{10} = -\frac{13k_1}{486}, \quad (87)$$

and hence we can write

$$E_{\text{ISCO}}^2 = 8/9 - \left(\frac{13k_1}{486}\right) \ell_{\text{P}}^2/R_{\text{S}}^2 + \text{O}(\ell_{\text{P}}^3/R_{\text{S}}^3), \quad (88)$$

which, jointly with either Eq. (79) or Eq. (80), permits obtaining the quantum corrected

ISCO radius

$$\mathcal{R}_{\text{ISCO}} = 3R_S - \left(\frac{25k_1}{36} \right) \ell_P^2/R_S + \mathcal{O}(\ell_P^3/R_S^2). \quad (89)$$

From the above relations, we find that the binding energy E_B per unit rest mass of the ISCO is

$$E_B = 1 - E_{\text{ISCO}} = 1 - \sqrt{8/9} \left[1 - \left(\frac{13k_1}{864} \right) \ell_P^2/R_S^2 + \mathcal{O}(\ell_P^3/R_S^3) \right]. \quad (90)$$

Similarly to the classical scenario, $V_t''(\mathcal{R}_{\text{ISCO}})$ vanishes up to higher-order corrections. In fact, by means of Eqs. (88) and (89), we find from Eq. (48b)

$$R_S^2 V_t''(\mathcal{R}_{\text{ISCO}}) = -\frac{k_1 \ell_P^2}{972 R_S^2} + \mathcal{O}(\ell_P^4/R_S^4), \quad (91)$$

which, when using the same numerical values as in Tables I and II for ℓ_P/R_S and k_1 , gives $R_S^2 V_t''(\mathcal{R}_{\text{ISCO}}) \sim 10^{-11}$.

In classical GR, the radii of UCOs and SCOs are subject to the conditions (56a) and (56b), respectively. Analogous constraints exist also in the quantum regime. In fact, as we have shown above, when $E_{\text{ISCO}}^2 \leq E^2 < 1$, SCOs have radius $\mathcal{R}_4 \geq \mathcal{R}_{\text{ISCO}}$. On the other hand, bearing in mind the classical result (57), the radius $\mathcal{R}_{\text{IUCO}}$ of the innermost UCO (located outside the black hole) could be found by solving Eq. (68) in the limit $E^2 \gg 1$ (while still complying with the requirement (82))³. Physically, $\mathcal{R}_{\text{IUCO}}$ should be equal to the radius of photon sphere, i.e., the unstable circular trajectory followed by photons. This actually occurs in our model, as when $E \gg 1$ Eq. (68) reduces to

$$\mathcal{R}^4 - \frac{3R_S}{2} \mathcal{R}^3 - \frac{3}{2} k_1 R_S \ell_P^2 \mathcal{R} + \frac{3}{2} k_1 R_S^2 \ell_P^2 = 0, \quad (92)$$

which takes *exactly* the same form as the equation pertaining to the photon sphere radius to be derived in Eq. (108) below. Therefore, a situation mirroring the classical scenario is valid also for UCOs, since

$$\mathcal{R}_{\text{IUCO}} < \mathcal{R}_3 < \mathcal{R}_{\text{ISCO}}, \quad (93)$$

with $E^2 > E_{\text{ISCO}}^2$ and $\mathcal{R}_{\text{IUCO}} \equiv \mathcal{R}_{\text{ps4}}$, see Eq. (110d) below.

Although the EFT scheme should be used with caution at scales of the order of the

³ Taking the limit $E^2 \gg 1$ in the solution (79) will not lead to the correct result, as this equation is not reliable when E^2 attains unboundedly large values.

Planck length, it can still offer a first rough account of quantum phenomena, giving rise to interesting scenarios. Indeed, one intriguing feature that distinguishes our model from classical general relativity is its prediction of (at least⁴) two disconnected SCO regions when $k_1 > 0$. In principle, bearing in mind Eq. (78a), there should exist SCOs with radius \mathcal{R}_1 residing in the black hole whenever $E^2 > 1 > E_{\text{ISCO}}^2$. However, our analysis shows that this happens if $E \gtrsim 1$, a situation which yields $\mathcal{R}_1 \lesssim \ell_{\text{P}}$. This can be inferred from Table I, where it is evident that when $E = 1.01$ we have $\mathcal{R}_1 \sim 10^{-1} \ell_{\text{P}}$, with $V_t''(\mathcal{R}_1) > 0$ and L^2 attaining a positive value; on the other hand, the solutions \mathcal{R}_1 with $E = 2$ and $E = 10$ lead to a negative L^2 , and hence must be regarded as nonphysical. Since $\mathcal{R}_1 < \tilde{r}_1$ (see Eq. (11)), the corresponding SCO trajectories cannot be observed from outside the black hole, and hence the potential physical inconsistencies deriving from the fact that \mathcal{R}_1 can become smaller than ℓ_{P} when $E \gtrsim 1$ present no issues.

Due to the presence of these inner SCO orbits, we can conclude that the pattern with positive k_1 features the presence of an ISCO located *deeply* inside the black hole (as first proved in Ref. [93]). Therefore, we can regard Eq. (89) as the quantum corrected version of the classical ISCO radius (59). This should be regarded as the “physical” ISCO, and hence hereafter we will refer to Eq. (89) as simply the ISCO.

An equivalent way to prove that the regime with $k_1 > 0$ allows for (at least) two disconnected SCO domains is as follows. If the SCO regions were connected, a SCO having radius \tilde{r}_1 would be viable. Therefore, the condition $V_t'(\tilde{r}_1) = 0$ would bring about the constraint

$$6k_1 [(2E^2 - 5) R_{\text{S}}^2 + 2L^2] + 4R_{\text{S}}^2 (L^2 + R_{\text{S}}^2) = 0. \quad (94)$$

Due to the relations (2) and (3), the above equation cannot be satisfied, and hence there exists no SCO with radius \tilde{r}_1 . This is of crucial physical importance: the null hypersurface at \tilde{r}_1 cannot serve as the site of a SCO, as such a scenario would imply that massive particles could seemingly escape from the black hole.

When $k_1 < 0$, both SCOs and UCOs are located outside the black hole, as they lie beyond the null hypersurface having radius \tilde{r}_3 (see Fig. 2). Indeed, in this case the solution \mathcal{R}_1 , which, when $E^2 < 1$, can be either of the order of ℓ_{P} or even smaller, yield a negative value of L^2 and hence is nonphysical (see table II).

⁴ The scenario with positive k_1 admits at least two disconnected SCO regions due to the presence of the two null hypersurfaces with radii \tilde{r}_1 and \tilde{r}_2 (see Eqs. (11) and (12)).

B. Massive particles trajectories

Since the effective potential (47) has, apart from L , an explicit dependence on the energy \mathcal{E} and the factor k_1 , the ensuing dynamics can manifest intriguing features in the quantum domain. In the classical scenario where $k_1 = 0$, the effective potential $V_t^{k_1=0}(r)$ is uniquely determined once the angular momentum L is fixed. Consequently, if there exists an UCO, a particle will fall into the black hole if its energy exceeds the value of the potential evaluated at the UCO radius, hereafter denoted with \mathcal{R}_{UCO} . This relation remains valid in the quantum realm as well, albeit \mathcal{R}_{UCO} receives an additional contribution from k_1 (notice that \mathcal{R}_{UCO} coincides with the physically meaningful solutions \mathcal{R}_3 , see Eq. (79)). Even though this quantum correction minimally affects the value of \mathcal{R}_{UCO} , it can lead to entirely different particle orbits even if identical initial conditions are chosen. This interesting phenomenon will be shown explicitly in this section.

The spatial orbits of massive particles can be easily derived starting from Eqs. (45) and (47), and then dividing the obtained formulas by $\dot{\phi} = L/r^2$ (which stems from the rotational invariance of the geometry (1)). In this way, we find that the equation governing the motion of massive bodies on the equatorial plane $\theta = \pi/2$ is

$$\left(\frac{dr}{d\phi}\right)^2 + \left(1 - \frac{R_S}{r}\right) \left(r^2 + \frac{r^4}{L^2}\right) + \frac{k_1 R_S \ell_P^2 r}{L^2} \left(\frac{3}{2} - \mathcal{E}^2\right) = \frac{r^4 \mathcal{E}^2}{L^2}. \quad (95)$$

In Figs. 7 and 8, we draw the trajectories resulting from Eq. (95) in the Euclidean plane, the coordinates x and y being defined in the usual way

$$x = r \cos \phi, \quad y = r \sin \phi. \quad (96)$$

In Fig. 7, although we have considered particles starting at the same location and with equal values of \mathcal{E} and L , we find that they exhibit opposite behaviors: the body trajectory falls into the black hole if $k_1 = -1$, whereas it returns almost to its initial position if $k_1 = 1$. This event should not be interpreted as a hint that the black hole with $k_1 = -1$ is more attractive than the one with $k_1 = 1$. Indeed, in Fig. 8, the situation is completely reversed: the particle plunges into the black hole if $k_1 = 1$, whereas it gets back to the initial position if $k_1 = -1$.

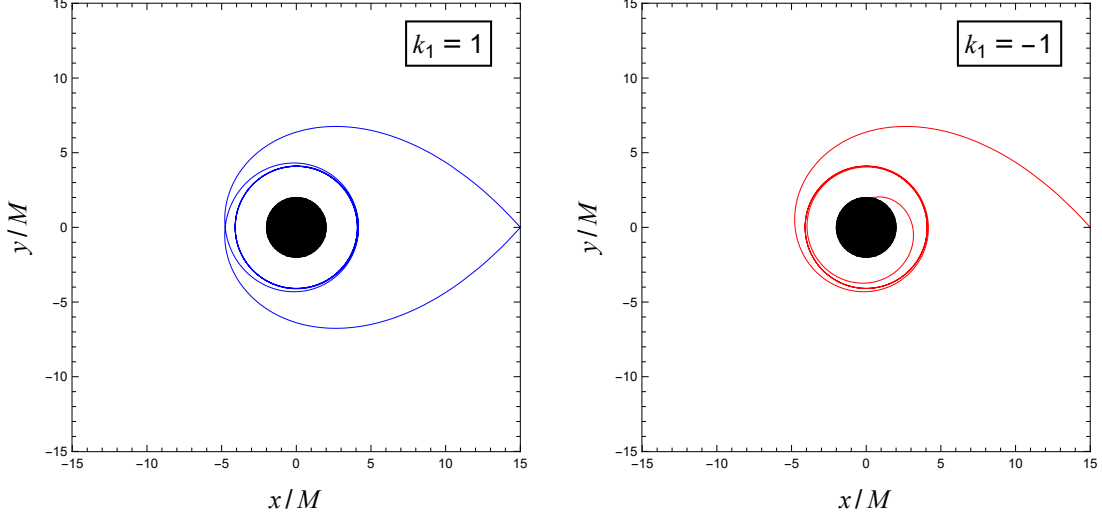


FIG. 7: Massive particle trajectories beginning at $x_0 = 15M, y_0 = 0$, with $\mathcal{E} = 0.99$ and $L = 3.918712113126M$ (we set $G = 1$). Although the initial conditions are the same, two distinct orbits are obtained: the body spirals into the black hole (represented by a black disk) or returns almost to its starting point, depending on whether $k_1 = 1$ or $k_1 = -1$, respectively. For both situations, we have $\ell_P/R_S = 10^{-4}$, which yields $\mathcal{R}_{\text{UCO}}^{k_1=1} = 2.044284344R_S$, $\mathcal{R}_{\text{UCO}}^{k_1=-1} = 2.044284345R_S$, and $V_t(\mathcal{R}_{\text{UCO}}^{k_1=1}) > \mathcal{E} > V_t(\mathcal{R}_{\text{UCO}}^{k_1=-1})$.

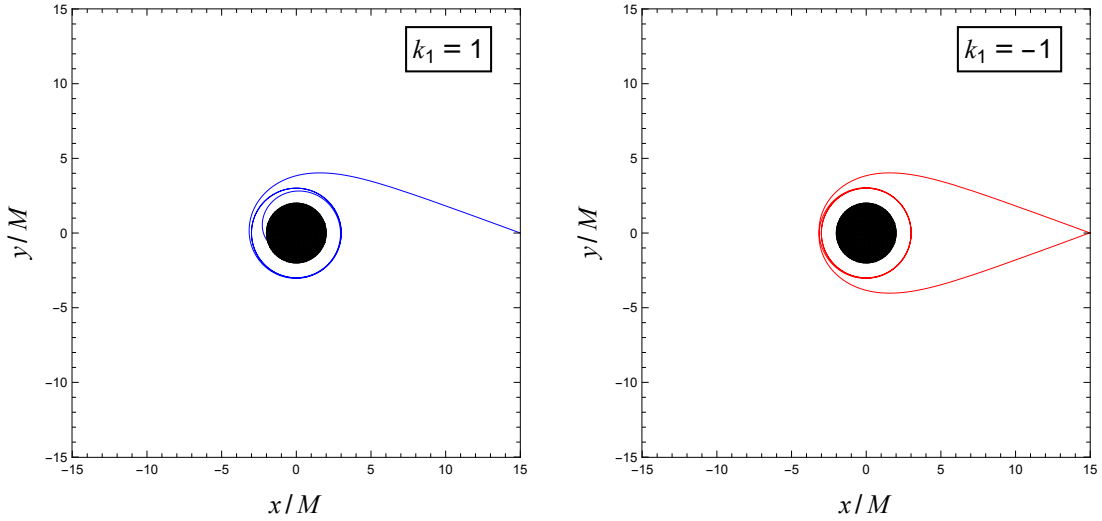


FIG. 8: Massive body paths starting at $x_0 = 15M, y_0 = 0$, with $\mathcal{E} = 10$ and $L = 51.8747440595M$ (we set $G = 1$). The particle either is drawn into the black hole or departs from it, depending on the sign of k_1 . Setting $\ell_P/R_S = 10^{-4}$, we have $\mathcal{R}_{\text{UCO}}^{k_1=1} = 1.50168R_S$, $\mathcal{R}_{\text{UCO}}^{k_1=-1} = 1.50171R_S$, and $V_t(\mathcal{R}_{\text{UCO}}^{k_1=1}) < \mathcal{E} < V_t(\mathcal{R}_{\text{UCO}}^{k_1=-1})$.

We stress that the only difference between these two configurations is represented by the values of L and \mathcal{E} , the latter meeting the constraint (82).

The interesting phenomenon presented in Figs. 7 and 8 cannot be used as mean to identify quantum signatures arising in the Schwarzschild geometry. Indeed, to be potentially

observed, we should be able to evaluate the factor $\Delta V_t := V_t(\mathcal{R}_{\text{UCO}}^{k_1 > 0}) - V_t(\mathcal{R}_{\text{UCO}}^{k_1 < 0})$. Since in general ΔV_t involves a lengthy expression, we will take for simplicity the cases $k_1 = \pm 1$ and $\mathcal{E} = 1, 2$. For $\mathcal{E} = 1$, we have from Eq. (64) that

$$\Delta V_t^{\mathcal{E}=1} = \frac{L^2 \ell_P^2}{64 R_S^4} + \mathcal{O}(\ell_P^4 / R_S^4), \quad (97)$$

while for $\mathcal{E} = 2$, we obtain owing to Eq. (79)

$$\begin{aligned} \Delta V_t^{\mathcal{E}=2} &= \frac{9 [174 (5\sqrt{7} - 14) L^2 + (743\sqrt{7} + 1834) R_S^2] \ell_P^2}{14 (\sqrt{7} + 2)^4 R_S^4} + \mathcal{O}(\ell_P^4 / R_S^4), \\ &\approx \frac{5.2438 \ell_P^2}{R_S^2} - \frac{0.1852 L^2 \ell_P^2}{R_S^4} + \mathcal{O}(\ell_P^4 / R_S^4). \end{aligned} \quad (98)$$

Bearing in mind that $\mathcal{R}_{\text{IUCO}} < \mathcal{R}_{\text{UCO}} < \mathcal{R}_{\text{ISCO}}$ (cf. Eq. (93)), we deduce from Eq. (52) that $L \sim \mathcal{E} R_S$, which allows us to conclude that

$$|\Delta V_t| \sim \ell_P^2 / R_S^2. \quad (99)$$

Now, consider the following *gedanken* experiment. Suppose that we prepare a light beam at some location r_0 outside the black hole, with its orbit determined by assigning specific values of \mathcal{E} and L . Initially, we set these initial conditions to produce light rays exhibiting the same unbounded trajectory for the two distinct quantum black hole models considered here, i.e., the one with $k_1 = 1$ and that with $k_1 = -1$. Subsequently, while keeping L fixed and increasing \mathcal{E} (or vice versa, i.e., fixing \mathcal{E} and decreasing L), we investigate whether the light beam maintains the same unbounded behavior for these two quantum black holes. This iterative process continues until distinct behaviors for the light beam emerge for the two different quantum black hole frameworks, as depicted in Figs. 7 and 8. In the final stage of this procedure, the relation (99) implies that the energy should be fine-tuned with extreme precision so that

$$\delta \mathcal{E} \lesssim \ell_P^2 / R_S^2, \quad (100)$$

or, equivalently, that the angular momentum should be measured with high accuracy, as

$$\delta L \lesssim \ell_{\text{P}}^2/R_{\text{S}} \ll \ell_{\text{P}}, \quad (101)$$

where the δ symbol refers to the difference in either \mathcal{E} or L in the two scenarios $k_1 = \pm 1$ mentioned above. Therefore, the search for possible detectable properties of the quantum Schwarzschild black hole via the dynamical behaviour displayed in Figs. 7 and 8 appears to be not feasible. Indeed, this would require a precision in the measurement process of \mathcal{E} and L which cannot be achieved, according to the basic principles of quantum mechanics [122]. A similar situation holds also for null geodesics, which will be studied in Sec. III C.

1. Radial geodesics

The motion of massive objects in radial free fall can be described via the effective potential

$$V_{\text{t}}^{\text{radial}}(r) = \frac{1}{2} \left(1 - \frac{R_{\text{S}}}{r} \right) + \frac{1}{2} k_1 \left(\frac{3}{2} - \mathcal{E}^2 \right) \frac{R_{\text{S}} \ell_{\text{P}}^2}{r^3}, \quad (102)$$

which can be promptly obtained from Eq. (47) with $L = 0$. In classical general relativity, where $k_1 = 0$, the effective potential always diverges towards negative infinity when r approaches zero, meaning that all bodies in the vicinity of $r = 0$ will be forced to plunge into the singularity. On the other hand, in the quantum regime the radial geodesics behavior near $r = 0$ is, in general, governed by the term proportional to k_1 . If we suppose that this quantum correction is valid also near $r = 0$, then interesting phenomena can happen at small scales. In fact, depending on the value of the energy, there exist particles which will never fall into the singularity. In particular, for $k_1 > 0$ this circumstance concerns bodies with $\mathcal{E}^2 < 3/2$, while when $k_1 < 0$ it occurs when $\mathcal{E}^2 > 3/2$ (particles with $\mathcal{E}^2 = 3/2$ will always be swallowed by the singularity if they happen to be close to $r = 0$, like in the classical scenario).

This event can be readily explained in the model with $k_1 > 0$, where (similarly to the Reissner-Nordström spacetime [123]) $r = 0$ is a timelike hypersurface (see Eq. (18a)), and hence it can be avoided by observers moving within the black hole (provided that $\mathcal{E}^2 < 3/2$, as we have just seen). Conversely, no classical arguments can account for this situation when

$k_1 < 0$, since in this case $r = 0$ is a spacelike hypersurface (see Eq. (19a)). Therefore, we can suppose that a particle is allowed to escape the singularity because of some antigravity effects taking place in the neighbourhood of $r = 0$. These would entail the presence of some quantum matter fields which lead to the breach of NEC in the scenario with $k_1 < 0$. Something similar occurs also when $k_1 > 0$. Indeed, as set out in Ref. [93], this geometrical setup permits the occurrence of a Penrose-like energy-extraction process which violates the Hawking area theorem and, as a consequence, the NEC. Therefore, as we discussed also in Sec. II C, we can conclude that in our model the NEC is not respected independently of the sign assumed by k_1 , a result that ties in with the quantum nature of the Schwarzschild geometry (1).

The validity of our considerations relies on the use of the EFT paradigm for scales where $r \approx 0$. Although, as pointed out before, strictly speaking the EFT scheme should not be invoked in this regime, it nevertheless can provide precious hints and a first rough estimation of physical phenomena involving quantum gravity effects at small scales. As evidence of this argument, our analysis seems to point toward the general expectation that the theory of quantum gravity should be able to resolve the singularity issues plaguing classical general relativity [124–126]. However, no possibility to assess the situations described in this section seems to be available, since they cannot be seen by any observer stationed outside the black hole.

C. Null geodesics

It is well-known that massless particles follow a path coinciding with a null geodesic [106]. Therefore, the dynamics of a photon can be described by setting $\alpha = 0$ in the formula (46) of the quantum corrected effective potential, thus obtaining (see Fig. 4)

$$V_n(r) = \frac{L^2}{2r^2} \left(1 - \frac{R_S}{r} \right) - k_1 \frac{\mathcal{E}^2 R_S \ell_P^2}{2r^3}. \quad (103)$$

In classical general relativity, the shape of the “null effective potential” is independent of L . On the other hand, in the quantum setting $V_n(r)$ receives a quantum contribution involving the energy \mathcal{E} . Despite that, we will see that the formulas of the quantum photon sphere radii involve neither \mathcal{E} nor L . This result, which has a fundamental physical significance,

will be proved in Sec. [IIIC1](#). Then, we conclude the section with the investigation of photon trajectories, see Sec. [IIIC2](#).

Similarly to the timelike geodesics case (see Eqs. [\(82\)](#) and [\(83\)](#)), our forthcoming analysis will be performed by taking into account the upper bound $\mathcal{E} \ll R_S/\ell_P$, which guarantees that quantum corrections to physical quantities never become as important as the classical ones, in agreement with the spirit of the EFT formalism.

1. The photon sphere

The photon sphere identifies the spacetime region where (unstable) circular light ray orbits are allowed. Its radius \mathcal{R}_{ps} can be thus identified by the maximum of the effective potential [\(103\)](#), i.e.,

$$V'_n(\mathcal{R}_{\text{ps}}) = 0, \quad (104)$$

which gives the expression

$$\mathcal{R}_{\text{ps}} = \frac{3R_S}{2} + \frac{3}{2}k_1 \frac{\mathcal{E}^2 R_S \ell_P^2}{L^2}. \quad (105)$$

The dependence on the ratio \mathcal{E}/L can be easily removed by resorting to the well-known identity (cf. Eq. [\(45\)](#))

$$V_n(\mathcal{R}_{\text{ps}}) = \frac{\mathcal{E}^2}{2}, \quad (106)$$

which yields the quantum corrected formula

$$\frac{\mathcal{E}^2}{L^2} = \frac{\mathcal{R}_{\text{ps}} - R_S}{\mathcal{R}_{\text{ps}}^3 + k_1 R_S \ell_P^2}. \quad (107)$$

Plugging the above relation into Eq. [\(105\)](#), we find the fourth-order algebraic equation

$$\mathcal{R}_{\text{ps}}^4 - \frac{3R_S}{2}\mathcal{R}_{\text{ps}}^3 - \frac{3}{2}k_1 R_S \ell_P^2 \mathcal{R}_{\text{ps}} + \frac{3}{2}k_1 R_S^2 \ell_P^2 = 0, \quad (108)$$

whose coefficients are independent of both the energy and angular momentum. For $k_1 = 0$, Eq. [\(108\)](#) reduces to a linear equation providing the single classical root

$$\bar{\mathcal{R}}_{\text{ps}4} = \frac{3R_S}{2}. \quad (109)$$

In the quantum regime having $k_1 \neq 0$, we can find the expanded version of the roots of the quartic (108) by applying the analytic method devised in Sec. III A for the examination of timelike geodesics. In this way, we get the following solutions:

$$\begin{aligned}\mathcal{R}_{\text{ps1}} &= \sqrt[3]{k_1} R_S (\ell_P/R_S)^{2/3} - \frac{k_1^{2/3} R_S}{9} (\ell_P/R_S)^{4/3} - \frac{2k_1 \ell_P^2}{27R_S} + \mathcal{O}\left(\ell_P^{8/3}/R_S^{5/3}\right), \\ \mathcal{R}_{\text{ps2}} &= -\sqrt[3]{-k_1} R_S (\ell_P/R_S)^{2/3} + \frac{(k_1)^{2/3} R_S}{9(-1)^{1/3}} (\ell_P/R_S)^{4/3} - \frac{2k_1 \ell_P^2}{27R_S} + \mathcal{O}\left(\ell_P^{8/3}/R_S^{5/3}\right), \\ \mathcal{R}_{\text{ps3}} &= (-1)^{2/3} \sqrt[3]{k_1} R_S (\ell_P/R_S)^{2/3} - \frac{k_1^{2/3} R_S}{9(-1)^{2/3}} (\ell_P/R_S)^{4/3} - \frac{2k_1 \ell_P^2}{27R_S} + \mathcal{O}\left(\ell_P^{8/3}/R_S^{5/3}\right), \\ \mathcal{R}_{\text{ps4}} &= \bar{\mathcal{R}}_{\text{ps4}} + \frac{2k_1 \ell_P^2}{9R_S} + \mathcal{O}\left(\ell_P^{8/3}/R_S^{5/3}\right),\end{aligned}\tag{110a}$$

$$\tag{110b}$$

$$\tag{110c}$$

$$\tag{110d}$$

where we note that \mathcal{R}_{ps1} , \mathcal{R}_{ps2} , and \mathcal{R}_{ps3} are fully quantum radii, consistently with the outcome of the classical analysis. It is easy to show that, up to higher-order terms in ℓ_P , the Viète formulas for the quartic equations are satisfied. Thus, not surprisingly, our analytic formulas (110) match closely with the numerical solutions, as witnessed by Tables III and IV.

Bearing in mind Eqs. (103) and (110d), we find

$$V_n''(\mathcal{R}_{\text{ps4}})/L^2 = -\left[9R_S^2(1 + 4k_1 \ell_P^2/b^2) - 4k_1 \ell_P^2\right] \frac{314928R_S^4}{(4k_1 \ell_P^2 + 27R_S^2)^5} + \mathcal{O}\left(\ell_P^{8/3}/R_S^{20/3}\right), \tag{111}$$

which is obviously negative in light of Eqs. (2) and (3). This means that \mathcal{R}_{ps4} is a maximum of the effective potential, and hence represents the radius of an UCO.

In principle, the roots of Eq. (108) can be: (i) all real, (ii) two real and two complex, (iii) all complex. The latter possibility is naturally ruled out, since the quartic (108) always admits at least one real-valued solution, i.e., the radius \mathcal{R}_{ps4} , which is the only one surviving in the classical limit. In addition, also the situation (i) is excluded. This is due to the fact that in Eqs. (110a)-(110c) the coefficient c_1 of the leading terms (i.e., those proportional

$$k_1 = 1, \ell_P/R_S = 10^{-1}$$

Solution	$\mathcal{R}_{\text{ps1}}/R_S$	$\mathcal{R}_{\text{ps2}}/R_S$	$\mathcal{R}_{\text{ps3}}/R_S$	$\mathcal{R}_{\text{ps4}}/R_S$
Analytic solution	0.20955	-0.10588-0.19105i	-0.10588+0.19105i	1.50222
Numerical solution	0.20945	-0.10584-0.19098i	-0.10584+0.19098i	1.50222

$$k_1 = 1, \ell_P/R_S = 10^{-2}$$

Solution	$\mathcal{R}_{\text{ps1}}/R_S$	$\mathcal{R}_{\text{ps2}}/R_S$	$\mathcal{R}_{\text{ps3}}/R_S$	$\mathcal{R}_{\text{ps4}}/R_S$
Analytic solution	0.04617	-0.02300-0.04041 i	-0.02300+0.04041i	1.50002
Numerical solution	0.04617	-0.02300-0.04041i	-0.02300+0.04041i	1.50002

$$k_1 = 1, \ell_P/R_S = 10^{-3}$$

Solution	$\mathcal{R}_{\text{ps1}}/R_S$	$\mathcal{R}_{\text{ps2}}/R_S$	$\mathcal{R}_{\text{ps3}}/R_S$	$\mathcal{R}_{\text{ps4}}/R_S$
Analytic solution	0.00999	-0.00400-0.00867i	-0.00400+0.00867i	1.50000
Numerical solution	0.00999	-0.00400-0.00867i	-0.00400+0.00867i	1.50000

$$k_1 = 1, \ell_P/R_S = 10^{-4}$$

Solution	$\mathcal{R}_{\text{ps1}}/R_S$	$\mathcal{R}_{\text{ps2}}/R_S$	$\mathcal{R}_{\text{ps3}}/R_S$	$\mathcal{R}_{\text{ps4}}/R_S$
Analytic solution	0.00215	-0.00108-0.00187i	-0.00108+0.00187i	1.50000
Numerical solution	0.00215	-0.00108-0.00187i	-0.00108+0.00187i	1.50000

TABLE III: Roots (in units of R_S) of the quartic (108) obtained analytically and numerically for $k_1 = 1$ and various values of ℓ_P/R_S . The results provided by our analytical approach align closely with the numerical findings.

to $\ell_P^{2/3}/R_S^{2/3}$) comes from the solutions of the equation $(c_1)^3 = k_1$, while the coefficient c_2 of the sub-leading corrections (which go like $\ell_P^{4/3}/R_S^{4/3}$) is given by the solutions of $(c_2)^3 = -k_1/(9c_1)$. If we recall that all nonzero real numbers have exactly one real cube root and a pair of complex conjugate cube roots, we soon realize that the case (i) is not present. Therefore, only the option (ii) is possible, as is clear also from Tables III and IV.

Our investigation reveals that there is one photon sphere radius when $k_1 < 0$ and two when $k_1 > 0$. This contrasts with classical general relativity, which predicts the existence of only one photon sphere, given by Eq. (109). In the quantum framework with k_1 positive, the radius \mathcal{R}_{ps1} lies deep inside the black hole and adheres to the relation $\mathcal{R}_{\text{ps1}} < \tilde{r}_1$ (see Eq. (11)), which means that it is not visible to any observer situated outside the black hole. In this way, the possible scenarios where $\mathcal{R}_{\text{ps1}} \lesssim \ell_P$ will not be experimentally accessible. On the other hand, orbits having radius \mathcal{R}_{ps4} are always visible, since $\mathcal{R}_{\text{ps4}} > \tilde{r}_1$ (case $k_1 > 0$) and $\mathcal{R}_{\text{ps4}} > \tilde{r}_3$ (case $k_1 < 0$), cf. Eqs. (11) and (16).

Contrary to the classical case, the effective potential (103) is nonvanishing when $L = 0$. This means that for scales where $r \approx 0$ and when $k_1 < 0$, radial photons do not reach the singularity at $r = 0$, despite its spacelike nature. A similar situation holds also for radial

$$k_1 = -1, \ell_P/R_S = 10^{-1}$$

Solution	$\mathcal{R}_{\text{ps1}}/R_S$	$\mathcal{R}_{\text{ps2}}/R_S$	$\mathcal{R}_{\text{ps3}}/R_S$	$\mathcal{R}_{\text{ps4}}/R_S$
Analytic solution	0.11104+0.18211i	0.11104-0.18211i	-0.21986	1.49778
Numerical solution	0.11108+0.18220i	0.11108+0.18220i	-0.21994	1.49778

$$k_1 = -1, \ell_P/R_S = 10^{-2}$$

Solution	$\mathcal{R}_{\text{ps1}}/R_S$	$\mathcal{R}_{\text{ps2}}/R_S$	$\mathcal{R}_{\text{ps3}}/R_S$	$\mathcal{R}_{\text{ps4}}/R_S$
Analytic solution	0.02334+0.03999i	0.02334-0.03999i	-0.04665	1.49998
Numerical solution	0.02334+0.03999i	0.02334-0.03999i	-0.04665	1.49998

$$k_1 = -1, \ell_P/R_S = 10^{-3}$$

Solution	$\mathcal{R}_{\text{ps1}}/R_S$	$\mathcal{R}_{\text{ps2}}/R_S$	$\mathcal{R}_{\text{ps3}}/R_S$	$\mathcal{R}_{\text{ps4}}/R_S$
Analytic solution	0.00501+0.00865i	0.00501-0.00865i	-0.01001	1.50000
Numerical solution	0.00501+0.00865i	0.00501-0.00865i	-0.01001	1.50000

$$k_1 = -1, \ell_P/R_S = 10^{-4}$$

Solution	$\mathcal{R}_{\text{ps1}}/R_S$	$\mathcal{R}_{\text{ps2}}/R_S$	$\mathcal{R}_{\text{ps3}}/R_S$	$\mathcal{R}_{\text{ps4}}/R_S$
Analytic solution	0.00108+0.00187i	0.00108-0.00187i	-0.00215	1.50000
Numerical solution	0.00108+0.00187i	0.00108-0.00187i	-0.00215	1.50000

TABLE IV: Roots (in units of R_S) of the quartic (108) for $k_1 = -1$ and different choices of ℓ_P/R_S . Our analytical approach and the numerics demonstrate strong agreement.

timelike geodesics (although only for certain values of the energy, see Sec. III B 1). The consequences that can be drawn from this phenomenon are thus similar.

2. Photon trajectories

It follows from Eqs. (45) and (103) that the spatial orbits followed by light rays on the equatorial plane $\theta = \pi/2$ of the Schwarzschild geometry (1) can be described by the equation

$$\left(\frac{dr}{d\phi}\right)^2 + \left(1 - \frac{R_S}{r}\right)r^2 - \frac{k_1 R_S \ell_P^2 r}{b^2} = \frac{r^4}{b^2}, \quad (112)$$

where we have exploited the relation $\dot{\phi} = L/r^2$ and the impact parameter is still defined as $b := L/\mathcal{E}$ (its physical meaning will be discussed in the Sec. IV). The ensuing trajectories are drawn in Figs. 9-11, where we have introduced Euclidean coordinates according to Eq. (96).

Quantum corrections bring forth intriguing novel facets into photon dynamics, similar to those examined for the timelike geodesic motion, which we have studied in Sec. III B. Let us hereafter set $G = 1$ for simplicity. In Fig. 9, we have considered a photon which

starts off its orbit from the point having coordinates $x_0 = 10M, y_0 = 0$, and with an impact parameter b which assumes the same value for both positive and negative k_1 cases. Since quantum modifications to the photon sphere radius change according to the sign assumed by k_1 (see Eq. (110d)), two kinds of trajectories are possible: the photon plunges into the black hole for $k_1 = 1$, while it approximately gets back to its initial position when $k_1 = -1$. A similar phenomenon is observed also in Figs. 10 and 11, albeit with different initial radii: $x_0 = 15M$ and $x_0 = 35M$, respectively. Therefore, our investigation shows that, although the photon sphere radius \mathcal{R}_{ps4} shows tiny deviations from its classical counterpart $\bar{\mathcal{R}}_{\text{ps4}}$, EFT theory predicts the occurrence of completely different motions even if identical initial conditions are chosen. This is a remarkable result, which, nevertheless, comes with a caveat:

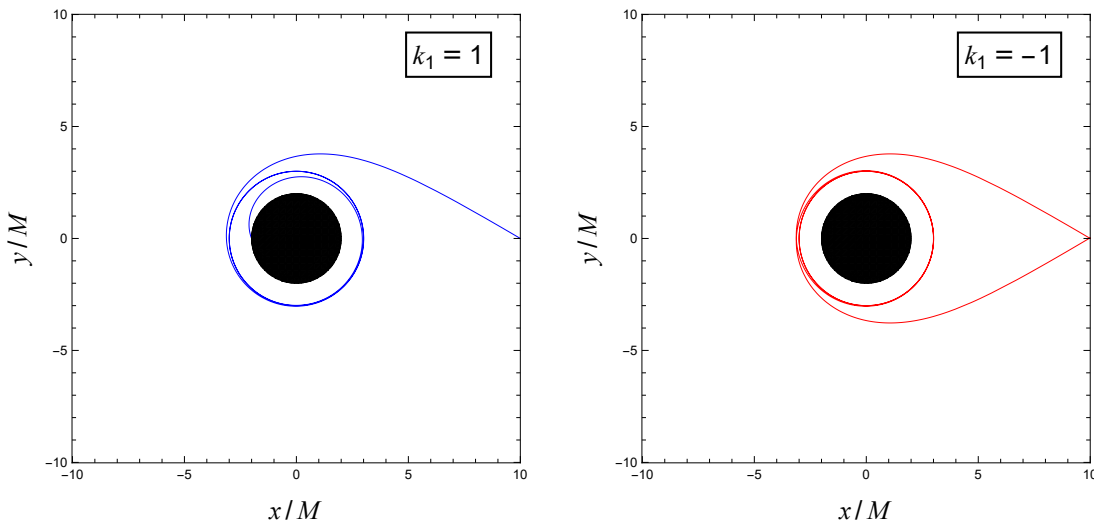


FIG. 9: Photon trajectories beginning at $x_0 = 10M, y_0 = 0$, with impact parameter $b = 5.19615191286M$. Despite having identical initial conditions, two distinct orbits are obtained: the photon falls into the black hole (represented by a black disk) or returns almost to its starting point, depending on whether $k_1 = 1$ or $k_1 = -1$, respectively. We set $\ell_{\text{P}}/R_{\text{S}} = 10^{-4}$ for both situations.

the opposite behaviours displayed in Figs. 9–11 do not permit the observation of quantum gravity signatures occurring at low-energy scales. As a consequence, the interesting features revealed in Figs. 9–11 cannot be employed to distinguish between frameworks with negative and positive k_1 . In fact, it follows from Eqs. (107) and (110d) that the impact parameter for the photon sphere at $r = \mathcal{R}_{\text{ps4}}$ is

$$b_{\text{ps4}} = \frac{3\sqrt{3}}{2}R_{\text{S}} + \frac{2k_1\ell_{\text{P}}^2}{3\sqrt{3}R_{\text{S}}} + \mathcal{O}(\ell_{\text{P}}^4/R_{\text{S}}^3), \quad (113)$$

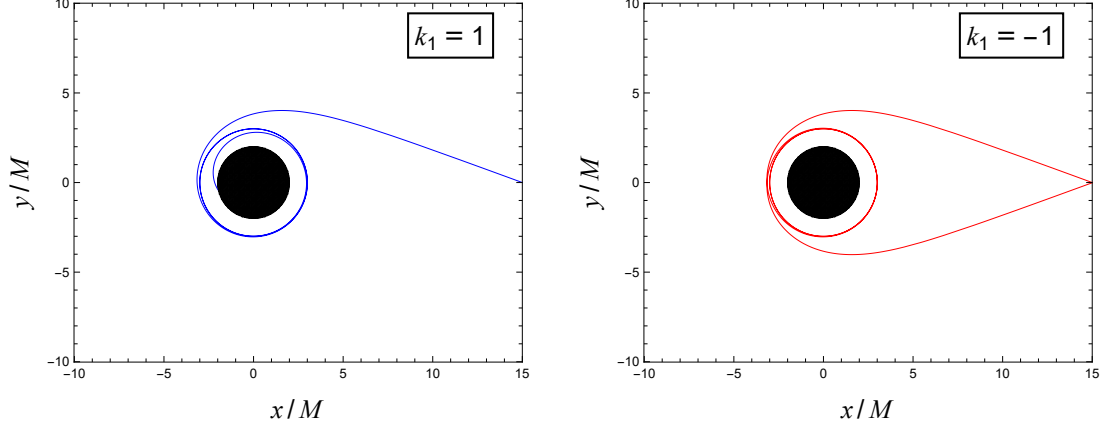


FIG. 10: Light ray trajectories starting at $x_0 = 15M, y_0 = 0$, with $b = 5.19615156261M$. The photon either enters the black hole or moves away from it, depending on the value assumed by k_1 . We set $\ell_P/R_S = 10^{-4}$ for both cases.

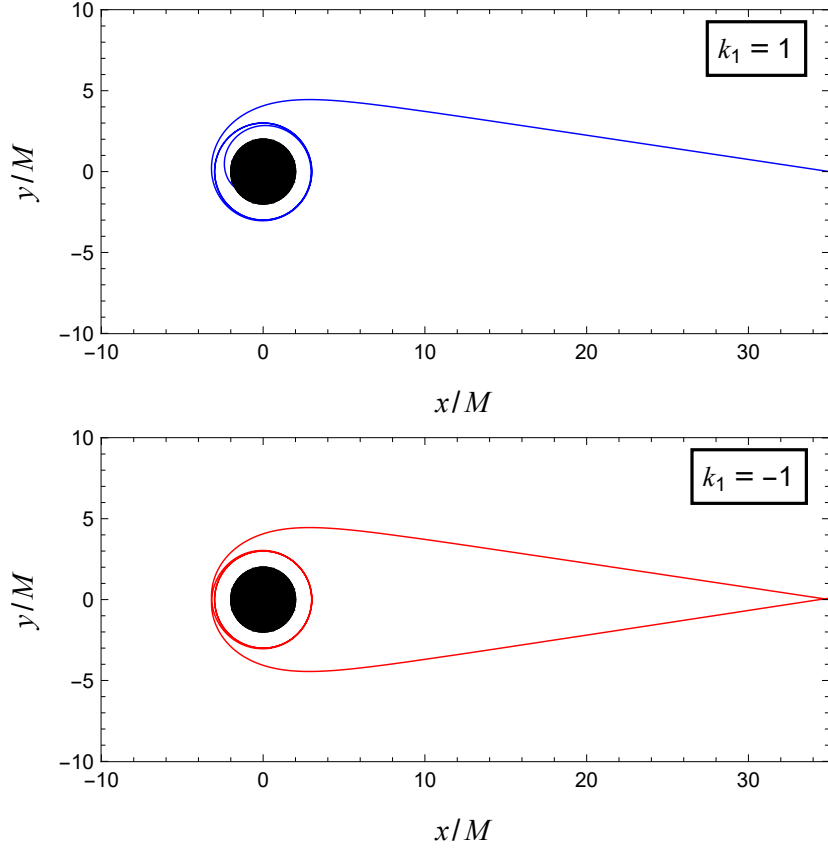


FIG. 11: Photon orbits with $x_0 = 35M, y_0 = 0$, and $b = 5.19615166247M$ showing that the motion is influenced by the sign of k_1 . We set $\ell_P/R_S = 10^{-4}$ for both situations.

which means that if

$$b_{\text{ps4}}^{k_1 < 0} \lesssim b \lesssim b_{\text{ps4}}^{k_1 > 0}, \quad (114)$$

then it would be possible to single out distinct photon trajectories on the basis of the sign of k_1 . However, such accuracy cannot be achieved, because it would require that the impact parameter be adjusted with extreme precision, as

$$b_{\text{ps4}}^{k_1>0} - b_{\text{ps4}}^{k_1<0} \lesssim \ell_{\text{P}}^2/R_S, \quad (115)$$

where we have used Eq. (2). Physically, this is not possible, as we have learned from quantum mechanics tenets [122]. However, while the net effect is far too small to be seen experimentally, we have found an interesting phenomenon in its own right.

At this stage, a final consideration is in order. Our analysis reveals an intriguing difference with massive particles dynamics. Indeed, the photon orbits displayed in Figs. 9–11 exhibit a trend similar to that depicted in Fig. 8, but not to the one occurring in Fig. 7. In particular, null geodesics having $k_1 = 1$ (which are sketched as blue curves) always cross the (outer) horizon, while the corresponding timelike curves can either depart from the black hole (Fig. 7) or move into it (Fig. 8).

IV. BLACK HOLE SHADOWS AND RINGS

The results provided in the previous section regarding the dynamics of both massive and massless particles have a wide range of applications. In particular, they enable the examination of the observational properties of the quantum black hole.

The landmark images of the supermassive black holes M87* and Sgr A*, recently released by the Event Horizon Telescope collaboration (EHT), have marked a significant milestone in gravitational physics [127–129]. This breakthrough achievement has put forth the notions of shadow and photon ring, which, due to their ability to provide crucial horizon-scale data, are used to test fundamental principles of gravity models in extreme environments and permit inferring key black hole information such as its mass, spin, and even its structure [130–136].

Black hole shadow corresponds to the central dark area revealed by the EHT images, whose theoretical size is intricately tied to the characteristics of the emission disk. Despite that, it is commonly associated with the apparent radius of the photon sphere, which for a distant observer in standard Schwarzschild geometry is given by $b_c = 3\sqrt{3}M$, with b_c the classical impact parameter corresponding to the classical photon sphere radius (109).

The photon ring is a region of enhanced brightness surrounding the black hole shadow and located near b_c .

According to the analysis performed in the previous section, both the ISCO and photon sphere radii receive quantum corrections depending on the constant k_1 . The ensuing emission features of the black hole are unavoidably influenced by these quantum terms and are thus studied in this section. Such aspects in fact allow us to further explore the consequences brought by the quantum modifications to the Schwarzschild geometry. After having provided some preliminary material in Sec. IV A, the emission profiles and appearance of the black hole will be addressed in Sec. IV B.

A. Preliminaries

The emission facets and the corresponding appearance of the black hole can be investigated by considering the light rays trajectories from the perspective of a distant observer, tracing them backward towards the vicinity of the black hole [130, 137]. For this reason, let us introduce the observer's local proper reference frame $(\hat{t}, \hat{r}, \hat{\theta}, \hat{\phi})$, which can be established by means of the non-coordinate orthonormal basis in the usual way [138]

$$\hat{e}_a = \partial/\partial\hat{x}^a = e_a^\mu (\partial/\partial x^\mu), \quad (116a)$$

with the dual basis satisfying

$$\hat{e}^a = d\hat{x}^a = e^a_\mu dx^\mu, \quad (116b)$$

where Latin (resp. Greek) letters denote frame (resp. coordinate) indices, and e_a^μ stand for the inverse of e^a_μ . The latter components are commonly referred to as tetrads or vielbeins, and form a 4×4 matrix with a positive determinant satisfying the orthonormality relation

$$g_{\mu\nu} = e^a_\mu e^b_\nu \eta_{ab}, \quad (117)$$

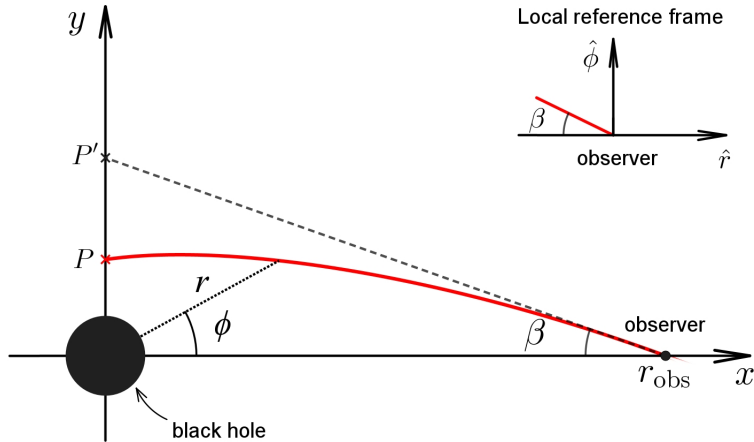


FIG. 12: Photon trajectory (red curve) in the equatorial plane $\theta = \pi/2$. The main figure exhibits the Euclidean coordinates x, y defined in Eq. (96), while the inset one showcases the local reference frame of the observer positioned at radius r_{obs} . The center of the black hole is positioned at the origin of the Euclidean plane. From the observer's perspective, light rays emitted from the point P seem to originate from point P' .

$\eta_{ab} = \text{diag}(-1, 1, 1, 1)$ being the Lorentz metric. When dealing with our spherically symmetric geometry (1), one readily obtains

$$e^a_{\mu} = \text{diag}(\sqrt{-g_{tt}}, \sqrt{g_{rr}}, \sqrt{g_{\theta\theta}}, \sqrt{g_{\phi\phi}}). \quad (118)$$

In Fig. 12, we depict a typical path followed by a photon as seen by an observer located at the radial distance r_{obs} . When viewed from the observer's standpoint, light emitted from the point P seems to originate from a different point P' . As a result, the perceived distance $y_{P'}$ from the center of the black hole differs from r_{obs} by a correcting factor, and reads as

$$y_{P'} = r_{\text{obs}} \tan \beta, \quad (119)$$

where the angular radius β is evaluated in the local frame as

$$\tan \beta = -d\hat{\phi}/d\hat{r}. \quad (120)$$

By means of the relation (116), one can write

$$\frac{d\hat{\phi}}{d\hat{r}} = \frac{r_{\text{obs}}}{\sqrt{A(r_{\text{obs}})}} \frac{d\phi}{dr} \Big|_{r_{\text{obs}}}, \quad (121)$$

and hence Eq. (112), jointly with formulas (120) and (121), permits to obtain

$$\tan^2 \beta = \frac{r_{\text{obs}}^2}{A(r_{\text{obs}})} \left[\frac{r_{\text{obs}}^4}{b^2} - \left(1 - \frac{R_S}{r_{\text{obs}}} \right) r_{\text{obs}}^2 + \frac{k_1 R_S \ell_P^2 r_{\text{obs}}}{b^2} \right]^{-1}, \quad (122)$$

which in turn yields

$$\sin^2 \beta = \frac{b^2 (r_{\text{obs}} - R_S)}{r_{\text{obs}}^3 [1 + \mathcal{O}(\ell_P^2 / r_{\text{obs}}^2)]}, \quad (123)$$

where we have employed Eq. (1c). For a distant observer, $r_{\text{obs}} \gg R_S$ and $\beta \ll 1$, and the above relations can be approximated as

$$\tan \beta \simeq \sin \beta \simeq b / r_{\text{obs}}, \quad (124)$$

which means that

$$y_{P'} \approx b := L / \mathcal{E}, \quad (125)$$

thus confirming that the factor b , first defined in Sec. III C 2, serves as the impact parameter for null geodesics reaching the observer at infinity.

In the subsequent analysis, b will be considered as the apparent distance of optical sources from the center of the black hole and we will assume that the observer is situated at $r_{\text{obs}} = 10^5 M$ with azimuthal angle $\phi = 0$.

B. Emission intensity profiles and black hole appearance

We are now ready to investigate simple scenarios where black hole emission originates from an optically and geometrically thin static disk located in its vicinity. The disk is observed face-on, and its specific intensity, denoted as I_ν (with ν representing the frequency of the emitted light in a static frame), depends solely on the radial coordinate r . The specific intensity emitted from the accretion disk is denoted as $I_{\text{em}}(r, \nu)$. As photons are emitted from the disk, the invariant intensity, $\mathcal{I}_\nu := I_\nu / \nu^3$, remains constant along their trajectories

in our framework, as all absorption mechanisms are neglected [130, 137]. Therefore, the specific intensity $I_{\text{obs}}(r_{\text{obs}}, \nu_{\text{obs}})$ received by the observer satisfies

$$\frac{I_{\text{em}}(r, \nu)}{I_{\text{obs}}(r_{\text{obs}}, \nu_{\text{obs}})} = \left(\frac{\nu}{\nu_{\text{obs}}} \right)^3 = \left[\frac{\mathcal{G}(r_{\text{obs}})}{\mathcal{G}(r)} \right]^3, \quad (126)$$

where $\mathcal{G}(r) := \sqrt{B(r)}$ is the redshift factor (see Eq. (1b)). For a distant observer, $r_{\text{obs}} \gg R_{\text{S}}$, and hence we have $\mathcal{G}(r_{\text{obs}}) \simeq 1$. Therefore, Eq. (126) boils down to

$$I_{\text{obs}}(r_{\text{obs}}, \nu_{\text{obs}}) = \mathcal{G}^3 I_{\text{em}}(r, \nu), \quad (127)$$

which implies that the total observed intensity resulting from light rays emitted from a specific location r can be integrated as

$$I_{\text{obs}}(r_{\text{obs}}) = \int I_{\text{obs}}(r_{\text{obs}}, \nu_{\text{obs}}) d\nu_{\text{obs}} = \int \mathcal{G}^4 I_{\text{em}}(r, \nu) d\nu = \mathcal{G}^4 I_{\text{em}}(r), \quad (128)$$

where $I_{\text{em}}(r) \equiv \int I_{\text{em}}(r, \nu) d\nu$ is the integrated intensity.

When tracing a light ray backward from the observer, there exists the possibility of intersecting the accretion disk, leading to an increase in brightness due to the disk emission. The frequency of such intersections determines the accumulated brightness along the ray's path. The total observed intensity is derived by summing the intensities contributed by each intersection [130]

$$I_{\text{obs}}(b) = \sum_m [\mathcal{G}^4 I_{\text{em}}] \Big|_{r=r_m(b)}, \quad (129)$$

where $r_m(b)$ ($m = 1, 2, 3, \dots$) denotes the radial coordinate of the m -th intersection position with the disk plane outside the black hole. For subsequent numerical computations, we will consider only the first three intersections.

Our investigation of the emission intensity profiles relies on the Gralla-Lupsasca-Marrone (GLM) model [132], which yields predictions closely aligned with those from general relativistic magneto-hydrodynamics simulations of astrophysical accretion disks [132, 139]. The

emission intensity profile of the GLM pattern is given by [132]

$$I_{\text{em}}(r) = \frac{e^{-\frac{1}{2}[\gamma + \text{arcsinh}(\frac{r-\mu}{\sigma})]^2}}{\sqrt{(r-\mu)^2 + \sigma^2}}, \quad (130)$$

where μ , γ , and σ are free phenomenological parameters governing the emission shape.

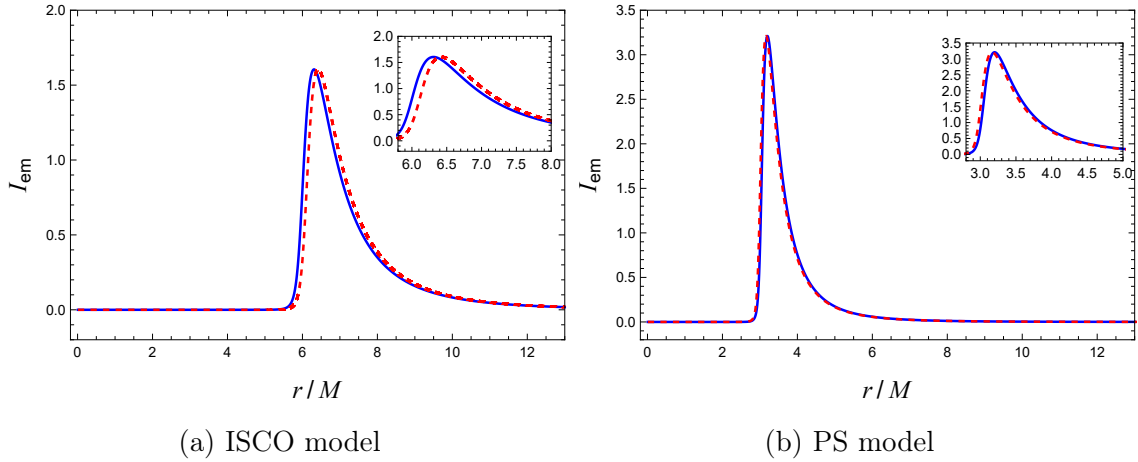


FIG. 13: ISCO and PS models given by Eq. (130). The blue and red dashed curves represent the emission intensity profiles for the black hole with $k_1 = 1$ and $k_1 = -1$, respectively. $\mathcal{R}_{\text{ISCO}}$ and \mathcal{R}_{ps4} have been evaluated by taking $\ell_{\text{P}}/R_{\text{S}} = 0.2$. The small boxes show zoomed-in details of the plots.

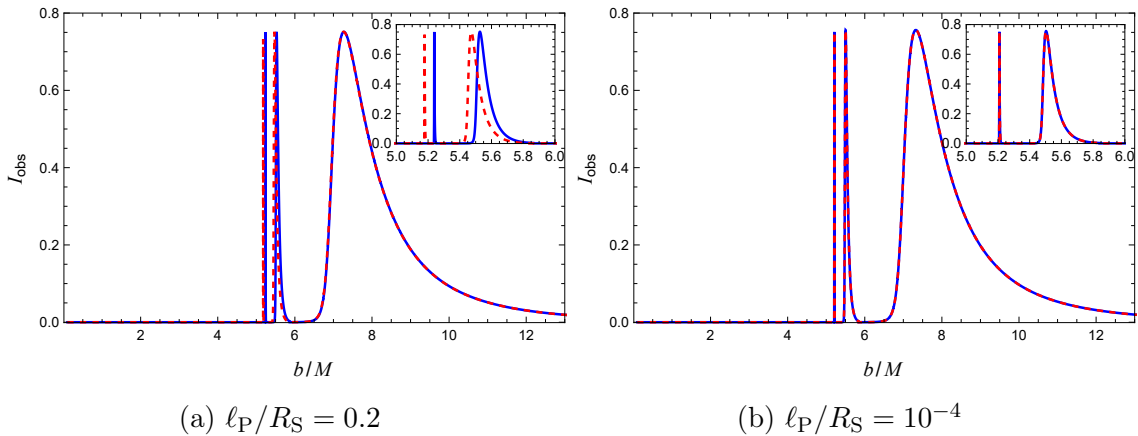


FIG. 14: Observed intensity (129) of the ISCO model for different values of the ratio $\ell_{\text{P}}/R_{\text{S}}$. The blue and red dashed curves represent the profile for the black hole with $k_1 = 1$ and $k_1 = -1$, respectively. The inset figures depict zoomed-in portions of the plots.

We will consider the following two different GLM profiles [132, 139, 140]:

- ISCO model: the emission graph is broadly peaked at the quantum radius $r = \mathcal{R}_{\text{ISCO}}$

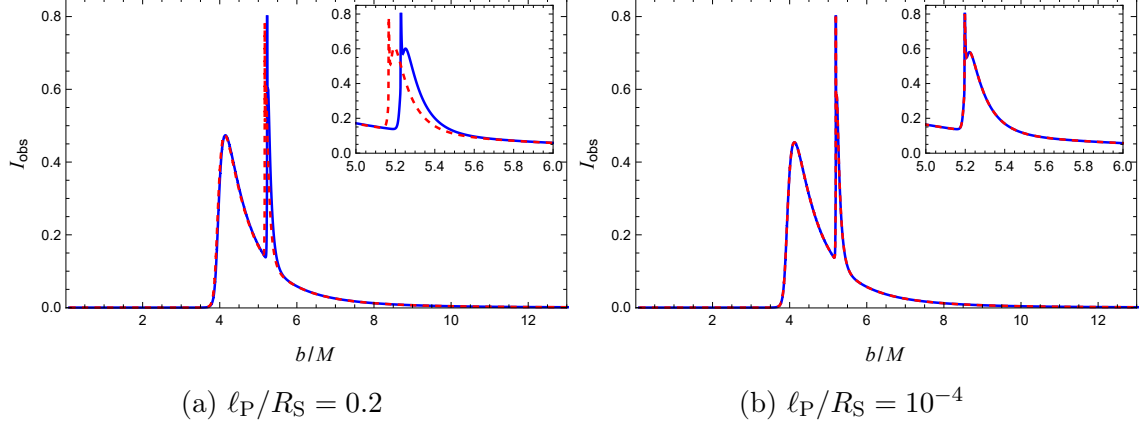


FIG. 15: Observed intensity (129) of the PS model for different values of the ratio ℓ_P/R_S . The blue and red dashed curves represent the profile for the black hole with $k_1 = 1$ and $k_1 = -1$, respectively. Small boxes within the figures display zoomed-in parts of the plots.

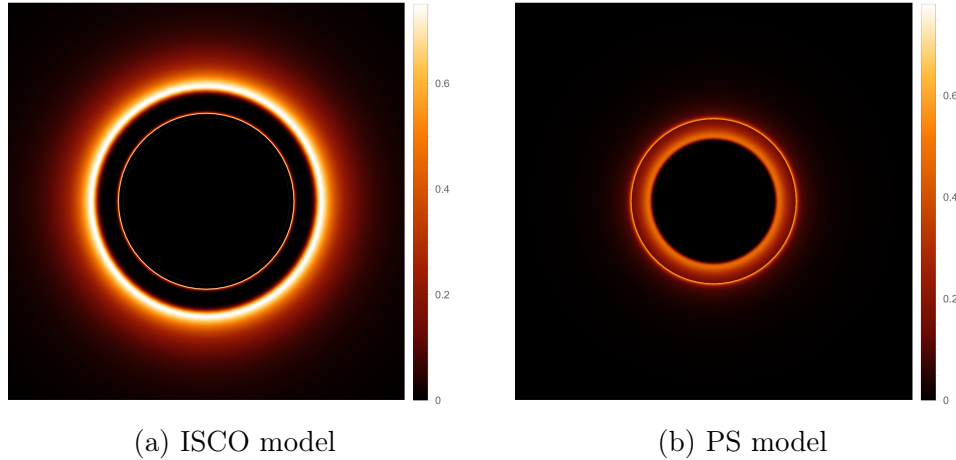


FIG. 16: Observational appearance for the ISCO and PS models of an optically thin disk of emission. We choose $\ell_P/R_S = 0.2$, and $k_1 = 1$ for left panel and $k_1 = -1$ for the right panel. Information regarding the observed intensity I_{obs} is reported on the right side of the figures. In the ISCO model, the photon ring appears as the thin circle within the dark area, while in the PS one, it appears as the outer ring surrounding the dark region.

(see Eq. (89)); minimal emission occurs when $r < \mathcal{R}_{\text{ISCO}}$, since in this region only UCOs are allowed, as we have shown previously. Following Ref. [132], for this framework we choose $\mu = \mathcal{R}_{\text{ISCO}}$, $\gamma = -2$, and $\sigma = M/4$.

- Photon sphere (PS) model: the emission curve peaks at the quantum position $r = \mathcal{R}_{\text{ps4}}$ (see Eq. (110d)), since there exist UCOs within the region $\mathcal{R}_{\text{ps4}} < r < \mathcal{R}_{\text{ISCO}}$, as we seen before. Inspired by Ref. [132], in this pattern we take $\mu = \mathcal{R}_{\text{ps4}}$, $\gamma = -2$, and $\sigma = M/8$.

The emission profiles and the observed appearances of the quantum Schwarzschild black hole are displayed in Figs. 13, and 14 – 16, respectively. It is clear that our analysis reveals tiny departures from the classical Schwarzschild solution, even in the limit scenario with $\ell_P/R_S = 0.2$. In other words, black hole shadows seem not to provide a mean to discriminate among the possible values of the factor k_1 occurring in the EFT literature devoted to study of quantum black hole geometries. In that regard, we also note that, for the scopes of this section, both the choice $\ell_P/R_S = 0.2$ and $\ell_P/R_S = 10^{-4}$ should be regarded as very extreme situations, although they still satisfy the constraint (3). Indeed, they yield primordial black holes having a mass $M \simeq 5 \times 10^{-8} \text{ kg} \sim 2.5 M_P$ in the first case, and $M \simeq 1 \times 10^{-4} \text{ kg} \sim 5 \times 10^4 M_P$ in the second.

V. CONCLUDING REMARKS

The issues related to the nonrenormalizability of Einstein theory can be overcome via the EFT approach, which permits to derive the leading one-loop long-distance quantum corrections arising in gravity interactions.

In this paper, we have analyzed the quantum Schwarzschild geometry within the EFT pattern. After having outlined its main facet along with some thermodynamic aspects in Sec. II, in Sec. III we have examined the behaviour of timelike and null geodesics. We have developed an efficient analytic method for solving the fourth-order algebraic equations governing the quantum positions of SCOs and UCOs. Consistently with the EFT recipes, the obtained roots are expressed in a readable way as a power series in the ratio ℓ_P/R_S , and have allowed us to compute the quantum version of the ISCO and PS radii (see Eqs. (78)–(80), (89), and (110)). In this way, we have discovered that the scenario having positive k_1 admits two disconnected SCO regions, and, as a consequence, a second ISCO radius, as well as two PS radii. These additional radii are located deep inside the black hole and are not visible from outside. Such characteristics are to be added to those already known from Sec. II A, i.e., the presence of two horizons and two null hypersurfaces where $g^{rr} = 0$. These can be regarded as drawbacks of the framework with $k_1 > 0$ when it is compared to the classical Schwarzschild solution.

The examination of massive and massless particles equations of motion has revealed an intriguing peculiarity of the quantum Schwarzschild black hole. Indeed, even if identical

initial conditions are chosen, the ensuing orbits exhibit different behaviours depending on the sign of k_1 (see Figs. 7, 8, and 9–11). This means that, although leading quantum contributions slightly alter the properties of the classical Schwarzschild spacetime, they can make causal geodesics evolve in completely different ways. Unfortunately, it appears that this phenomenon yields no direct observable signatures of the quantum corrections affecting the dynamics, and hence cannot be exploited to single out the possible values of k_1 occurring in the quantum Schwarzschild metric (1).

In Sec. IV, we have considered a first application of the results concerning the geodesic motion by dealing with black hole shadows and rings, which have garnered considerable interest in the recent literature since the groundbreaking images disclosed by EHT collaboration. Similarly as before, quantum imprints in the ISCO and PS emission profiles seem to indicate no visible consequences (see Figs. 13–16).

One interesting aspect of the quantum Schwarzschild solution is that the effective potential (46) depends explicitly on the energy. Such characteristic has allowed us to work out a cutoff energy scale for our model involving the ratio R_S/ℓ_P , or equivalently M/M_P (see Eqs. (82) and (83)). This ties in with the principles of EFT scheme, which entail that new particles or degrees of freedom become important at specific energy scales. Broadly speaking, energy-dependent quantum effects can have different origins and lead to significant implications. First of all, they can hint at the need for renormalization procedures and indicate the running of coupling constants, which are known to be basic ingredients of a quantum field theory. Furthermore, they can also be connected with phenomena like the quantum tunneling, which influences the behavior of particles in potential wells.

The results obtained in this paper can trigger the study of further relevant topics. In particular, a key point to be addressed concerns the search for quantum phenomena which can give rise to some measurable outcomes. This circumstance will permit to determine the correct value of the k_1 factor, thereby resolving the discrepancies in the existing literature. Our analysis seems to point toward the case with $k_1 < 0$, which however is plagued by the fact that it predicts no bounds on the mass M , while the other paradigm naturally implements the constraint (4) (recall in fact that the horizons (5) and (6) can be defined only if $M > M^* \sim M_P$). These subjects, along with the investigation of other fundamental properties of the quantum Schwarzschild black hole, deserve a careful consideration in a separate paper.

ACKNOWLEDGEMENTS

The work of Z. W. is supported by the Natural Science Foundation of Jiangsu Province (BK20220642). E. B. acknowledges the support of INFN *sezione di Napoli, iniziativa specifica* QGSKY and Moonlight2. E. B. thanks D-IAS for the hospitality and support. E. B. thanks Dr. R. Marotta for useful discussions and clarifications on some of the topics investigated in the paper.

- [1] M. E. Peskin and D. V. Schroeder, *An Introduction to quantum field theory*. Addison-Wesley, Reading, USA, 1995.
- [2] G. 't Hooft and M. J. G. Veltman, “One loop divergencies in the theory of gravitation,” *Ann. Inst. H. Poincare Phys. Theor. A* **20** (1974) 69–94.
- [3] M. H. Goroff and A. Sagnotti, “The Ultraviolet Behavior of Einstein Gravity,” *Nucl. Phys. B* **266** (1986) 709–736.
- [4] P. van Nieuwenhuizen and C. C. Wu, “On Integral Relations for Invariants Constructed from Three Riemann Tensors and their Applications in Quantum Gravity,” *J. Math. Phys.* **18** (1977) 182.
- [5] C. Rovelli, *Quantum gravity*. Cambridge Monographs on Mathematical Physics. Univ. Pr., Cambridge, UK, 2004.
- [6] A. Ashtekar and J. Pullin, eds., *Loop Quantum Gravity: The First 30 Years*, vol. 4 of *100 Years of General Relativity*. World Scientific, 2017.
- [7] O. Aharony, S. S. Gubser, J. M. Maldacena, H. Ooguri, and Y. Oz, “Large N field theories, string theory and gravity,” *Phys. Rept.* **323** (2000) 183–386, [arXiv:hep-th/9905111](#).
- [8] K. Becker, M. Becker, and J. H. Schwarz, *String theory and M-theory: A modern introduction*. Cambridge University Press, 12, 2006.
- [9] R. Blumenhagen, D. Lüüst, and S. Theisen, *Basic concepts of string theory*. Theoretical and Mathematical Physics. Springer, Heidelberg, Germany, 2013.
- [10] R. Penrose, “The Twistor Program,” *Rept. Math. Phys.* **12** (1977) 65–76.
- [11] A. Connes and M. Marcolli, *Noncommutative Geometry, Quantum Fields and Motives*. 2008.

- [12] H. C. Steinacker, *Quantum Geometry, Matrix Theory, and Gravity*. Cambridge University Press, 4, 2024.
- [13] G. Esposito, *Quantum gravity, quantum cosmology and Lorentzian geometries*, vol. 12. 1992.
- [14] G. Esposito, A. Y. Kamenshchik, and G. Pollifrone, *Euclidean quantum gravity on manifolds with boundary*, vol. 85. Springer, Dordrecht, Germany, 1997.
- [15] R. Loll, “Quantum Gravity from Causal Dynamical Triangulations: A Review,” *Class. Quant. Grav.* **37** no. 1, (2020) 013002, [arXiv:1905.08669 \[hep-th\]](#).
- [16] S. Surya, “The causal set approach to quantum gravity,” *Living Rev. Rel.* **22** no. 1, (2019) 5, [arXiv:1903.11544 \[gr-qc\]](#).
- [17] J. F. Donoghue, “General relativity as an effective field theory: The leading quantum corrections,” *Phys. Rev. D* **50** (1994) 3874–3888, [arXiv:gr-qc/9405057](#).
- [18] J. F. Donoghue, “Introduction to the effective field theory description of gravity,” in *Advanced School on Effective Theories*. 6, 1995. [arXiv:gr-qc/9512024](#).
- [19] J. F. Donoghue, “The effective field theory treatment of quantum gravity,” *AIP Conf. Proc.* **1483** no. 1, (2012) 73–94, [arXiv:1209.3511 \[gr-qc\]](#).
- [20] J. F. Donoghue, M. M. Ivanov, and A. Shkerin, “EPFL Lectures on General Relativity as a Quantum Field Theory,” [arXiv:1702.00319 \[hep-th\]](#).
- [21] E. Battista, *Extreme Regimes in Quantum Gravity*. Nova Science Publishers, Hauppauge, New York, 2017.
- [22] B. Latosh, *Effective theories of gravity*. PhD thesis, Sussex U., 2019.
- [23] C. P. Burgess, *Introduction to Effective Field Theory*. Cambridge University Press, 12, 2020.
- [24] J. F. Donoghue, “Quantum General Relativity and Effective Field Theory,” [arXiv:2211.09902 \[hep-th\]](#).
- [25] N. E. J. Bjerrum-Bohr, L. Planté, and P. Vanhove, *Effective Field Theory and Applications*. 2024.
- [26] J. F. Donoghue, “Leading quantum correction to the Newtonian potential,” *Phys. Rev. Lett.* **72** (1994) 2996–2999, [arXiv:gr-qc/9310024](#).
- [27] I. B. Khriplovich and G. G. Kirilin, “Quantum power correction to the Newton law,” *J. Exp. Theor. Phys.* **95** no. 6, (2002) 981–986, [arXiv:gr-qc/0207118](#).
- [28] N. E. J. Bjerrum-Bohr, J. F. Donoghue, and B. R. Holstein, “Quantum gravitational corrections to the nonrelativistic scattering potential of two masses,” *Phys. Rev. D* **67**

- (2003) 084033, [arXiv:hep-th/0211072](#). [Erratum: Phys.Rev.D 71, 069903 (2005)].
- [29] T. de Paula Netto, L. Modesto, and I. L. Shapiro, “Universal leading quantum correction to the Newton potential,” *Eur. Phys. J. C* **82** no. 2, (2022) 160, [arXiv:2110.14263 \[hep-th\]](#).
- [30] M. B. Fröb, C. Rein, and R. Verch, “Graviton corrections to the Newtonian potential using invariant observables,” *JHEP* **01** (2022) 180, [arXiv:2109.09753 \[hep-th\]](#).
- [31] J. F. Donoghue, B. R. Holstein, B. Garbrecht, and T. Konstandin, “Quantum corrections to the Reissner-Nordström and Kerr-Newman metrics,” *Phys. Lett. B* **529** (2002) 132–142, [arXiv:hep-th/0112237](#). [Erratum: Phys.Lett.B 612, 311–312 (2005)].
- [32] N. E. J. Bjerrum-Bohr, J. F. Donoghue, and B. R. Holstein, “Quantum corrections to the Schwarzschild and Kerr metrics,” *Phys. Rev. D* **68** (2003) 084005, [arXiv:hep-th/0211071](#). [Erratum: Phys.Rev.D 71, 069904 (2005)].
- [33] E. Battista and G. Esposito, “Restricted three-body problem in effective-field-theory models of gravity,” *Phys. Rev. D* **89** no. 8, (2014) 084030, [arXiv:1402.2931 \[gr-qc\]](#).
- [34] E. Battista and G. Esposito, “Full three-body problem in effective-field-theory models of gravity,” *Phys. Rev. D* **90** no. 8, (2014) 084010, [arXiv:1407.3545 \[gr-qc\]](#). [Erratum: Phys.Rev.D 93, 049901 (2016)].
- [35] E. Battista, S. Dell’Agnello, G. Esposito, and J. Simo, “Quantum effects on Lagrangian points and displaced periodic orbits in the Earth-Moon system,” *Phys. Rev. D* **91** (2015) 084041, [arXiv:1501.02723 \[gr-qc\]](#). [Erratum: Phys.Rev.D 93, 049902 (2016)].
- [36] E. Battista, S. Dell’Agnello, G. Esposito, L. Di Fiore, J. Simo, and A. Grado, “Earth-moon Lagrangian points as a test bed for general relativity and effective field theories of gravity,” *Phys. Rev. D* **92** (2015) 064045, [arXiv:1507.02902 \[gr-qc\]](#). [Erratum: Phys.Rev.D 93, 109904 (2016)].
- [37] A. Tartaglia, G. Esposito, E. Battista, S. Dell’Agnello, and B. Wang, “Looking for a new test of general relativity in the solar system,” *Mod. Phys. Lett. A* **33** no. 24, (2018) 1850136, [arXiv:1801.07236 \[gr-qc\]](#).
- [38] A. A. Ansari, S. Alhowaity, E. I. Abouelmagd, and S. K. Sahdev, “Analysis of Equilibrium Points in Quantized Hill System,” *Mathematics* **10** no. 13, (2022) .
- [39] E. Battista, A. Tartaglia, G. Esposito, D. Lucchesi, M. L. Ruggiero, P. Valko, S. Dell’Agnello, L. Di Fiore, J. Simo, and A. Grado, “Quantum time delay in the gravitational field of a rotating mass,” *Class. Quant. Grav.* **34** no. 16, (2017) 165008,

- [arXiv:1703.08095 \[gr-qc\]](#).
- [40] J.-W. Kim, “Quantum corrections to frame-dragging in scattering amplitudes,” *Phys. Rev. D* **106** no. 8, (2022) L081901, [arXiv:2207.04970 \[hep-th\]](#).
- [41] E. Battista, G. Esposito, and A. Tartaglia, “An effective-gravity perspective on the Sun–Jupiter–comet three-body system,” *Int. J. Geom. Meth. Mod. Phys.* **17** no. 11, (2020) 2050168, [arXiv:1910.14551 \[gr-qc\]](#).
- [42] A. Alshaery and E. I. Abouelmagd, “Analysis of the spatial quantized three-body problem,” *Results in Physics* **17** (2020) 103067.
<https://www.sciencedirect.com/science/article/pii/S2211379720302990>.
- [43] J. Singh, E. I. Abouelmagd, V. S. Kalantonis, and A. E. Perdiou, “A Quantized Hill’s Dynamical System,” *Advances in Astronomy* **2021** (2021) 9963761.
- [44] E. I. Abouelmagd, J. L. García Guirao, and J. Llibre, “Periodic Orbits of Quantised Restricted Three-Body Problem,” *Universe* **9** no. 3, (2023) 149.
- [45] K. Yamada and H. Asada, “Collinear solution to the general relativistic three-body problem,” *Phys. Rev. D* **82** (2010) 104019, [arXiv:1010.2284 \[gr-qc\]](#).
- [46] K. Yamada and H. Asada, “Uniqueness of collinear solutions for the relativistic three-body problem,” *Phys. Rev. D* **83** (2011) 024040, [arXiv:1011.2007 \[gr-qc\]](#).
- [47] T. Ichita, K. Yamada, and H. Asada, “Post-Newtonian effects on Lagrange’s equilateral triangular solution for the three-body problem,” *Phys. Rev. D* **83** (2011) 084026, [arXiv:1011.3886 \[gr-qc\]](#).
- [48] K. Yamada, T. Tsuchiya, and H. Asada, “Post-Newtonian effects on the stability of the triangular solution in the three-body problem for general masses,” *Phys. Rev. D* **91** no. 12, (2015) 124016, [arXiv:1505.04534 \[gr-qc\]](#).
- [49] Y. Nakamura and H. Asada, “Collinear and triangular solutions to the coplanar and circular three-body problem in the parametrized post-Newtonian formalism,” *Phys. Rev. D* **107** no. 4, (2023) 044005, [arXiv:2212.00198 \[gr-qc\]](#).
- [50] A. C. Jenkins, A. G. A. Pithis, and M. Sakellariadou, “Can we detect quantum gravity with compact binary inspirals?,” *Phys. Rev. D* **98** no. 10, (2018) 104032, [arXiv:1809.06275 \[gr-qc\]](#).
- [51] H.-Y. Liu, Y.-S. Piao, and J. Zhang, “Probing higher-spin particles with gravitational waves from compact binary inspirals,” [arXiv:2302.08042 \[gr-qc\]](#).

- [52] R. Mandal, S. Gangopadhyay, and A. Lahiri, “Newtonian cosmology from quantum corrected Newtonian potential,” *Phys. Lett. B* **839** (2023) 137807, [arXiv:2212.07913 \[gr-qc\]](#).
- [53] B. Latosh and A. Yachmenev, “On two body gravitational scattering within perturbative gravity,” *Class. Quant. Grav.* **40** no. 24, (2023) 245008, [arXiv:2304.08812 \[gr-qc\]](#).
- [54] B. Latosh, “Beyond Horndeski interactions induced by quantum effects,” *Mod. Phys. Lett. A* **36** no. 37, (2021) 2150258, [arXiv:2102.08025 \[hep-th\]](#).
- [55] A. Arbuzov and B. Latosh, “Effective potential of scalar–tensor gravity,” *Class. Quant. Grav.* **38** no. 1, (2021) 015012, [arXiv:2007.06306 \[hep-th\]](#).
- [56] B. Latosh, “One-loop effective scalar-tensor gravity,” *Eur. Phys. J. C* **80** no. 9, (2020) 845, [arXiv:2004.00927 \[hep-th\]](#).
- [57] R. Ali, R. Babar, H. Aounallah, and A. Övgün, “First-order quantum correction of thermodynamics in a charged accelerating AdS black hole with gauge potential,” *Int. J. Geom. Meth. Mod. Phys.* **21** no. 08, (2024) 2450149.
- [58] B. Latosh, “FeynGrav: FeynCalc extension for gravity amplitudes,” *Class. Quant. Grav.* **39** no. 16, (2022) 165006, [arXiv:2201.06812 \[hep-th\]](#).
- [59] B. N. Latosh, “FeynGrav and Recent Progress in Computational Perturbative Quantum Gravity,” *Symmetry* **16** no. 1, (2024) 117, [arXiv:2401.05608 \[hep-th\]](#).
- [60] N. E. J. Bjerrum-Bohr, J. F. Donoghue, and P. Vanhove, “On-shell Techniques and Universal Results in Quantum Gravity,” *JHEP* **02** (2014) 111, [arXiv:1309.0804 \[hep-th\]](#).
- [61] N. E. J. Bjerrum-Bohr, P. H. Damgaard, G. Festuccia, L. Planté, and P. Vanhove, “General Relativity from Scattering Amplitudes,” *Phys. Rev. Lett.* **121** no. 17, (2018) 171601, [arXiv:1806.04920 \[hep-th\]](#).
- [62] N. E. J. Bjerrum-Bohr, P. H. Damgaard, L. Planté, and P. Vanhove, “Classical gravity from loop amplitudes,” *Phys. Rev. D* **104** no. 2, (2021) 026009, [arXiv:2104.04510 \[hep-th\]](#).
- [63] P. H. Damgaard and P. Vanhove, “Remodeling the effective one-body formalism in post-Minkowskian gravity,” *Phys. Rev. D* **104** no. 10, (2021) 104029, [arXiv:2108.11248 \[hep-th\]](#).
- [64] N. E. J. Bjerrum-Bohr, P. H. Damgaard, L. Planté, and P. Vanhove, “Classical gravity from loop amplitudes,” *Phys. Rev. D* **104** no. 2, (2021) 026009, [arXiv:2104.04510 \[hep-th\]](#).

- [65] P. Vanhove, “An S-matrix approach to gravitational-wave physics,” *Phil. Trans. Roy. Soc. Lond. A* **380** no. 2230, (2022) 20210181.
- [66] I. Dymnikova, “Vacuum nonsingular black hole,” *Gen. Rel. Grav.* **24** (1992) 235–242.
- [67] A. Bonanno and M. Reuter, “Renormalization group improved black hole space-times,” *Phys. Rev. D* **62** (2000) 043008, [arXiv:hep-th/0002196](#).
- [68] S. A. Hayward, “Formation and evaporation of regular black holes,” *Phys. Rev. Lett.* **96** (2006) 031103, [arXiv:gr-qc/0506126](#).
- [69] G. G. Kirilin, “Quantum corrections to the Schwarzschild metric and reparametrization transformations,” *Phys. Rev. D* **75** (2007) 108501, [arXiv:gr-qc/0601020](#).
- [70] C. González and B. Koch, “Improved Reissner–Nordström–(A)dS black hole in asymptotic safety,” *Int. J. Mod. Phys. A* **31** no. 26, (2016) 1650141, [arXiv:1508.01502 \[hep-th\]](#).
- [71] X. Calmet and B. K. El-Menoufi, “Quantum Corrections to Schwarzschild Black Hole,” *Eur. Phys. J. C* **77** no. 4, (2017) 243, [arXiv:1704.00261 \[hep-th\]](#).
- [72] P. Bargueño, S. Bravo Medina, M. Nowakowski, and D. Batic, “Quantum Mechanical Corrections to the Schwarzschild Black Hole Metric,” *EPL* **117** no. 6, (2017) 60006, [arXiv:1605.06463 \[gr-qc\]](#).
- [73] A. Ashtekar, J. Olmedo, and P. Singh, “Quantum Transfiguration of Kruskal Black Holes,” *Phys. Rev. Lett.* **121** no. 24, (2018) 241301, [arXiv:1806.00648 \[gr-qc\]](#).
- [74] X. Calmet, R. Casadio, and F. Kuipers, “Quantum Gravitational Corrections to a Star Metric and the Black Hole Limit,” *Phys. Rev. D* **100** no. 8, (2019) 086010, [arXiv:1909.13277 \[hep-th\]](#).
- [75] P. Nicolini, E. Spallucci, and M. F. Wondrak, “Quantum Corrected Black Holes from String T-Duality,” *Phys. Lett. B* **797** (2019) 134888, [arXiv:1902.11242 \[gr-qc\]](#).
- [76] A. Platania, “Dynamical renormalization of black-hole spacetimes,” *Eur. Phys. J. C* **79** no. 6, (2019) 470, [arXiv:1903.10411 \[gr-qc\]](#).
- [77] V. Faraoni and A. Giusti, “Unsettling physics in the quantum-corrected Schwarzschild black hole,” *Symmetry* **12** no. 8, (2020) 1264, [arXiv:2006.12577 \[gr-qc\]](#).
- [78] O. Ruiz and E. Tuiran, “Nonperturbative quantum correction to the Reissner-Nordström spacetime with running Newton’s constant,” *Phys. Rev. D* **107** no. 6, (2023) 066003, [arXiv:2112.12519 \[gr-qc\]](#).

- [79] X. Calmet and F. Kuipers, “Quantum gravitational corrections to the entropy of a Schwarzschild black hole,” *Phys. Rev. D* **104** no. 6, (2021) 066012, [arXiv:2108.06824 \[hep-th\]](#).
- [80] A. Eichhorn and A. Held, “Black holes in asymptotically safe gravity and beyond,” [arXiv:2212.09495 \[gr-qc\]](#).
- [81] A. D’Alise, G. Fabiano, D. Frattulillo, S. Hohenegger, D. Iacobacci, F. Pezzella, and F. Sannino, “Positivity Conditions for Generalised Schwarzschild Space-Times,” [arXiv:2305.12965 \[gr-qc\]](#).
- [82] M. Del Piano, S. Hohenegger, and F. Sannino, “Quantum black hole physics from the event horizon,” *Phys. Rev. D* **109** no. 2, (2024) 024045, [arXiv:2307.13489 \[gr-qc\]](#).
- [83] P. Beltrán-Palau, A. del Río, and J. Navarro-Salas, “Quantum corrections to the Schwarzschild metric from vacuum polarization,” *Phys. Rev. D* **107** no. 8, (2023) 085023, [arXiv:2212.08089 \[gr-qc\]](#).
- [84] H. Gong, S. Li, D. Zhang, G. Fu, and J.-P. Wu, “Quasinormal modes of quantum-corrected black holes,” [arXiv:2312.17639 \[gr-qc\]](#).
- [85] S. Mitra, S. Chakraborty, R. Vicente, and J. C. Feng, “Probing the quantum nature of black holes with ultra-light boson environments,” [arXiv:2312.06783 \[gr-qc\]](#).
- [86] P. H. Damgaard and K. Lee, “The Schwarzschild Black Hole from Perturbation Theory to all Orders,” [arXiv:2403.13216 \[hep-th\]](#).
- [87] M. Del Piano, S. Hohenegger, and F. Sannino, “Effective Metric Descriptions of Quantum Black Holes,” [arXiv:2403.12679 \[gr-qc\]](#).
- [88] J. Lin, M. Bravo-Gaete, and X. Zhang, “Quasinormal modes, greybody factors and thermodynamics of four dimensional AdS black holes in Critical Gravity,” [arXiv:2401.02045 \[gr-qc\]](#).
- [89] S. U. Khan, U. Uktamov, J. Rayimbaev, A. Abdujabbarov, I. Ibragimov, and Z.-M. Chen, “Circular orbits and collisions of particles with magnetic dipole moment near magnetized Kerr black holes in modified gravity,” *Eur. Phys. J. C* **84** no. 2, (2024) 203.
- [90] P. Bhar, D. J. Gogoi, and S. Ponglertsakul, “Noncommutative black hole in de Rham-Gabadadze-Tolley like massive gravity,” [arXiv:2404.10627 \[gr-qc\]](#).
- [91] D. Hooper, G. Krnjaic, and S. D. McDermott, “Dark Radiation and Superheavy Dark Matter from Black Hole Domination,” *JHEP* **08** (2019) 001, [arXiv:1905.01301 \[hep-ph\]](#).

- [92] J. M. Maldacena, “Eternal black holes in anti-de Sitter,” *JHEP* **04** (2003) 021, [arXiv:hep-th/0106112](#).
- [93] E. Battista, “Quantum Schwarzschild geometry in effective field theory models of gravity,” *Phys. Rev. D* **109** no. 2, (2024) 026004, [arXiv:2312.00450 \[gr-qc\]](#).
- [94] V. Ferrari, L. Gualtieri, and P. Pani, *General Relativity and its Applications*. CRC Press, Taylor & Francis Group, 2020.
- [95] G. W. Gibbons and J. B. Hartle, “Real Tunneling Geometries and the Large Scale Topology of the Universe,” *Phys. Rev. D* **42** (1990) 2458–2468.
- [96] T. Dereli, M. Onder, and R. W. Tucker, “Signature transitions in quantum cosmology,” *Class. Quant. Grav.* **10** (1993) 1425–1434.
- [97] M. Bojowald and S. Brahma, “Loop quantum gravity, signature change, and the no-boundary proposal,” *Phys. Rev. D* **102** no. 10, (2020) 106023, [arXiv:2011.02884 \[gr-qc\]](#).
- [98] J. W. Barrett, G. W. Gibbons, M. J. Perry, C. N. Pope, and P. Ruback, “Kleinian geometry and the N=2 superstring,” *Int. J. Mod. Phys. A* **9** (1994) 1457–1494, [arXiv:hep-th/9302073](#).
- [99] M. Mars, J. M. M. Senovilla, and R. Vera, “Signature change on the brane,” *Phys. Rev. Lett.* **86** (2001) 4219–4222, [arXiv:gr-qc/0012099](#).
- [100] A. Stern and C. Xu, “Signature change in matrix model solutions,” *Phys. Rev. D* **98** no. 8, (2018) 086015, [arXiv:1808.07963 \[hep-th\]](#).
- [101] I. Bars, C. Deliduman, and O. Andreev, “Gauged duality, conformal symmetry and space-time with two times,” *Phys. Rev. D* **58** (1998) 066004, [arXiv:hep-th/9803188](#).
- [102] I. Bars, “Gravity in 2T-Physics,” *Phys. Rev. D* **77** (2008) 125027, [arXiv:0804.1585 \[hep-th\]](#).
- [103] I. Bars and J. Terning, *Extra dimensions in space and time*. 2010.
- [104] A. Kamenshchik and F. Muscolino, “Looking for Carroll particles in two time spacetime,” *Phys. Rev. D* **109** no. 2, (2024) 025005, [arXiv:2310.19050 \[hep-th\]](#).
- [105] M. S. Morris and K. S. Thorne, “Wormholes in space-time and their use for interstellar travel: A tool for teaching general relativity,” *Am. J. Phys.* **56** (1988) 395–412.
- [106] R. M. Wald, *General Relativity*. Chicago Univ. Pr., Chicago, USA, 1984.

- [107] R. M. Wald, “The thermodynamics of black holes,” *Living Rev. Rel.* **4** (2001) 6, [arXiv:gr-qc/9912119](#).
- [108] D. V. Fursaev, “Temperature and entropy of a quantum black hole and conformal anomaly,” *Phys. Rev. D* **51** (1995) 5352–5355, [arXiv:hep-th/9412161](#).
- [109] R.-G. Cai, L.-M. Cao, and N. Ohta, “Black Holes in Gravity with Conformal Anomaly and Logarithmic Term in Black Hole Entropy,” *JHEP* **04** (2010) 082, [arXiv:0911.4379 \[hep-th\]](#).
- [110] B. K. El-Menoufi, “Quantum gravity of Kerr-Schild spacetimes and the logarithmic correction to Schwarzschild black hole entropy,” *JHEP* **05** (2016) 035, [arXiv:1511.08816 \[hep-th\]](#).
- [111] Y. Xiao and Y. Tian, “Logarithmic correction to black hole entropy from the nonlocality of quantum gravity,” *Phys. Rev. D* **105** no. 4, (2022) 044013, [arXiv:2104.14902 \[gr-qc\]](#).
- [112] R. M. Wald, “Black hole entropy is the Noether charge,” *Phys. Rev. D* **48** no. 8, (1993) R3427–R3431, [arXiv:gr-qc/9307038](#).
- [113] V. Iyer and R. M. Wald, “Some properties of Noether charge and a proposal for dynamical black hole entropy,” *Phys. Rev. D* **50** (1994) 846–864, [arXiv:gr-qc/9403028](#).
- [114] I. Teimouri, *On Aspects of Infinite Derivatives Field Theories & Infinite Derivative Gravity*. PhD thesis, Lancaster U., 2018. [arXiv:1811.09818 \[gr-qc\]](#).
- [115] N. E. J. Bjerrum-Bohr, J. F. Donoghue, B. R. Holstein, L. Planté, and P. Vanhove, “Bending of Light in Quantum Gravity,” *Phys. Rev. Lett.* **114** no. 6, (2015) 061301, [arXiv:1410.7590 \[hep-th\]](#).
- [116] N. E. J. Bjerrum-Bohr, J. F. Donoghue, B. R. Holstein, L. Plante, and P. Vanhove, “Light-like Scattering in Quantum Gravity,” *JHEP* **11** (2016) 117, [arXiv:1609.07477 \[hep-th\]](#).
- [117] D. Bai and Y. Huang, “More on the Bending of Light in Quantum Gravity,” *Phys. Rev. D* **95** no. 6, (2017) 064045, [arXiv:1612.07629 \[hep-th\]](#).
- [118] H.-H. Chi, “Graviton Bending in Quantum Gravity from One-Loop Amplitudes,” *Phys. Rev. D* **99** no. 12, (2019) 126008, [arXiv:1903.07944 \[hep-th\]](#).
- [119] R. B. King and E. R. Canfield, “An algorithm for calculating the roots of a general quintic equation from its coefficients,” *Journal of Mathematical Physics* **32** no. 4, (Apr., 1991) 823–825.

- [120] S. Chandrasekhar, *The mathematical theory of black holes*. 1985.
- [121] M. Abramowitz, I. A. Stegun, *et al.*, *Handbook of mathematical functions*, vol. 10. Dover, New York, 1968.
- [122] G. Esposito, G. Marmo, G. Miele, and G. Sudarshan, *Advanced concepts in quantum mechanics*. Cambridge University Press, 10, 2014.
- [123] E. Poisson, *A Relativist's Toolkit: The Mathematics of Black-Hole Mechanics*. Cambridge University Press, 12, 2009.
- [124] I. Kuntz and R. Casadio, “Singularity avoidance in quantum gravity,” *Phys. Lett. B* **802** (2020) 135219, [arXiv:1911.05037 \[hep-th\]](#).
- [125] R. Carballo-Rubio, F. Di Filippo, S. Liberati, and M. Visser, “Geodesically complete black holes,” *Phys. Rev. D* **101** (2020) 084047, [arXiv:1911.11200 \[gr-qc\]](#).
- [126] R. Carballo-Rubio, S. Liberati, and V. Vellucci, “Geodesically complete universes,” [arXiv:2404.13112 \[gr-qc\]](#).
- [127] **Event Horizon Telescope** Collaboration, K. Akiyama *et al.*, “First M87 Event Horizon Telescope Results. I. The Shadow of the Supermassive Black Hole,” *Astrophys. J. Lett.* **875** (2019) L1, [arXiv:1906.11238 \[astro-ph.GA\]](#).
- [128] **Event Horizon Telescope** Collaboration, K. Akiyama *et al.*, “First M87 Event Horizon Telescope Results. VI. The Shadow and Mass of the Central Black Hole,” *Astrophys. J. Lett.* **875** no. 1, (2019) L6, [arXiv:1906.11243 \[astro-ph.GA\]](#).
- [129] **Event Horizon Telescope** Collaboration, K. Akiyama *et al.*, “First Sagittarius A* Event Horizon Telescope Results. I. The Shadow of the Supermassive Black Hole in the Center of the Milky Way,” *Astrophys. J. Lett.* **930** no. 2, (2022) L12, [arXiv:2311.08680 \[astro-ph.HE\]](#).
- [130] S. E. Gralla, D. E. Holz, and R. M. Wald, “Black Hole Shadows, Photon Rings, and Lensing Rings,” *Phys. Rev. D* **100** no. 2, (2019) 024018, [arXiv:1906.00873 \[astro-ph.HE\]](#).
- [131] R. Narayan, M. D. Johnson, and C. F. Gammie, “The Shadow of a Spherically Accreting Black Hole,” *Astrophys. J. Lett.* **885** no. 2, (2019) L33, [arXiv:1910.02957 \[astro-ph.HE\]](#).
- [132] S. E. Gralla, A. Lupasca, and D. P. Marrone, “The shape of the black hole photon ring: A precise test of strong-field general relativity,” *Phys. Rev. D* **102** no. 12, (2020) 124004, [arXiv:2008.03879 \[gr-qc\]](#).

- [133] T.-T. Sui, Z.-L. Wang, and W.-D. Guo, “The effect of scalar hair on the charged black hole with the images from accretions disk,” *Eur. Phys. J. C* **84** no. 4, (2024) 441, [arXiv:2311.10946 \[gr-qc\]](#).
- [134] H.-X. Jiang, C. Liu, I. K. Dihinia, Y. Mizuno, H. Xu, T. Zhu, and Q. Wu, “Shadows of Loop Quantum Black Holes: Semi-analytical Simulations of Loop Quantum Gravity Effects on Sagittarius A* and M 87*,” [arXiv:2312.04288 \[gr-qc\]](#).
- [135] J.-P. Ye, Z.-Q. He, A.-X. Zhou, Z.-Y. Huang, and J.-H. Huang, “Shadows and photon rings of a quantum black hole,” [arXiv:2312.17724 \[gr-qc\]](#).
- [136] L. You, Y.-H. Feng, R.-B. Wang, J.-B. Deng, and X.-R. Hu, “Decoding quantum gravity information with black hole accretion disk,” [arXiv:2404.01418 \[gr-qc\]](#).
- [137] Z.-L. Wang, “Shadows and rings of a de Sitter–Schwarzschild black hole,” *Eur. Phys. J. Plus* **138** no. 12, (2023) 1131, [arXiv:2307.12361 \[gr-qc\]](#).
- [138] M. Nakahara, *Geometry, topology and physics*. 2003.
- [139] J. L. Rosa, C. F. B. Macedo, and D. Rubiera-Garcia, “Imaging compact boson stars with hot spots and thin accretion disks,” *Phys. Rev. D* **108** no. 4, (2023) 044021, [arXiv:2303.17296 \[gr-qc\]](#).
- [140] J. L. Rosa, “Observational properties of relativistic fluid spheres with thin accretion disks,” *Phys. Rev. D* **107** no. 8, (2023) 084048, [arXiv:2302.11915 \[gr-qc\]](#).